



A Novel Optimal Time Window Determination Approach for ISAR Imaging of Ship Targets

Rui Cao , Graduate Student Member, IEEE, Yong Wang , Senior Member, IEEE, Chunmao Yeh, Yun Zhang, Member, IEEE, and Xiaofei Lu 

Abstract—A well-focused and high-resolution inverse synthetic aperture radar (ISAR) image of ship target is appropriate to the target classification and recognition, especially for the ISAR image presenting the ship’s top or side view. For this purpose, a novel optimal time window determination (OTWD) approach based on the imaging projection plane (IPP) selection is proposed in this article. First, the proposed OTWD approach determines the view of ship target in the ISAR image via the IPP selection. Then, the Doppler frequency is estimated via the time-frequency distribution (TFD) calculation for the azimuth signal of one scatterer. For the case of one range bin with multiple scatterers, a novel TFD extraction approach based on the clustering analysis is proposed. Afterward, the Doppler frequency is analyzed with sharpness to determine the optimal imaging time window, which can ensure the high image quality and optimal azimuth resolution. The proposed OTWD method is verified as accurate and effective with the experiments on simulated and real measured data.

Index Terms—Doppler frequency analysis, imaging projection plane (IPP), inverse synthetic aperture radar (ISAR), optimal time window, sharpness analysis, ship imaging.

NOMENCLATURE

ISAR	Inverse synthetic aperture radar.
IPP	Imaging projection plane.
RD	Range Doppler.
TWL	Time window length.
TFD	Time-frequency distribution.
OTWD	Optimal time window determination.
RLOS	Radar line of sight.
SPWVD	Smoothed pseudo Wigner-Ville distribution.
PRF	Pulse repetition frequency.
HCA	Hierarchical clustering algorithm.
O-RPY	Ship coordinate system.
O-UVW	Radar coordinate system.
\mathbf{r}	Coordinate of the static scatterer A in O-RPY.

Manuscript received November 3, 2021; revised December 25, 2021; accepted January 4, 2022. Date of publication March 22, 2022; date of current version May 11, 2022. This work was supported in part by the National Natural Science Foundation of China under Grant 61871146, and in part by the Fundamental Research Funds for the Central Universities under Grant FRFCU5710093720. (Corresponding author: Yong Wang.)

Rui Cao, Yong Wang, and Yun Zhang are with the Research Institute of Electronic Engineering Technology, Harbin Institute of Technology, Harbin 150001, China (e-mail: caor@hit.edu.cn; wangyong6012@hit.edu.cn; zhangyunhit@hit.edu.cn).

Chunmao Yeh is with the Beijing Institute of Radio Measurement, Beijing 100854, China (e-mail: ycm05@mails.thu.edu.cn).

Xiaofei Lu is with the Jiuquan Satellite Launch Center, Jiuquan 732750, China (e-mail: luxf08@163.com).

Digital Object Identifier 10.1109/JSTARS.2022.3161204

θ_i	Rotation angle in a direction, $i = r, p, y$.
i	Representing direction of axis R, P , or Y .
$\tilde{\mathbf{r}}(t_m)$	Coordinate of the rotating scatterer A in O-RPY.
t_m	Slow time.
\mathbf{R}_r	Rotation matrix in 3-D direction.
$\mathbf{R}_{\text{roll}}(\theta_r)$	Rotation matrix in roll direction.
$\mathbf{R}_{\text{pitch}}(\theta_p)$	Rotation matrix in pitch direction.
$\mathbf{R}_{\text{yaw}}(\theta_y)$	Rotation matrix in yaw direction.
$\mathbf{u}(t_m)$	Coordinate of the rotating scatterer A in O-UVW.
$\mathbf{R}_T(\varphi_u)$	Transform matrix with the angle φ_u .
φ_u	Angle between the axis U and R .
$s_r(t_m)$	Azimuth signal of the scatterer A.
$a_a(t_m)$	Amplitude modulation function.
λ	Wavelength.
$R_A(t_m)$	Range between the scatterer A and radar.
$-u_r$	U -axis coordinate of the radar in O-UVW.
\mathbf{u}_0	Coordinate of the static scatterer A in O-UVW.
θ_j	Rotation angle in a direction, $j = u, v, w$.
j	Representing direction of the axis U, V , or W .
T_w	Time window.
ω_j	Rotation angular velocity, $j = u, v, w$.
ω_i	Rotation angular velocity, $i = r, p, y$.
ω_e	Effective rotation angular velocity.
γ	Angle between vector ω_e and ω_v .
$\boldsymbol{\omega}_a$	Synthesis rotation vector.
\mathbf{m}	Normal vector of plane VOW in O-UVW.
β	Angle between vector $\boldsymbol{\omega}_a$ and plane VOW.
$f_d^A(t_m)$	Doppler frequency of the scatterer A.
$f_d^\Delta(t_m)$	Doppler frequency difference.
u_Δ	Range difference.
k_s	Slope value of the ship centerline.
$\boldsymbol{\omega}_u^1$	Unit vector in the direction of RLOS.
$\tilde{\mathbf{n}}$	Normal vector of azimuth direction.
x_a	Azimuth position of scatterer.
Δx_a	Azimuth position difference of ship target.
Δv_{A0}	Length of ship target in the axis V .
Δw_{A0}	Length of ship target in the axis W .
Δf_d	Doppler spread.
$s_r(m, n)$	Discrete echo data, $m = 1, 2, \dots, N_a$, $n = 1, 2, \dots, N_r$.
N_a	Azimuth bin number of echo data.
N_r	Range bin number of echo data.
m	Azimuth order.
n	Range order.
$s_r^q(m, n)$	q th discrete echo subdata, $m = 1, 2, \dots, N_{as}$.

N_{as}	Azimuth bin number of echo subdata.
$F(\cdot)$	Function of ship centerline extraction approach.
$C(\cdot)$	Function of pixel sum on a line.
ρ	Polar radius.
ρ_w	Accumulation width.
ρ_0	Initial polar radius.
\mathbf{H}_0	Matrix generated via Hough transform.
\mathbf{H}_w	Matrix after accumulating width.
N_w	Maximum number extracted from \mathbf{H}_w .
$\hat{\rho}_w$	Optimal accumulation width, ship width.
$\hat{\theta}$	Optimal accumulation direction; slope value.
D_{\max}	Maximum azimuth bin of ship in ISAR image.
D_{\min}	Minimum azimuth bin of ship in ISAR image.
D_w	Number of Doppler broadening bin.
$s_r^E(m, n)$	Extended subdata.
ρ_a	Azimuth resolution of ISAR image.
$\Delta\theta$	Rotation angle during the time window.
A	Rotation amplitude.
τ	Rotation period.
ϕ	Initial rotation phase.
$f_d(m)$	Doppler frequency.
\mathbf{F}_m	Range of Doppler frequency at azimuth bin m .
$f_{d\min}^m$	Minimum value of \mathbf{F}_m .
$f_{d\max}^m$	Maximum value of \mathbf{F}_m .
$S(m, f_n)$	Function of SPWVD.
$g(\cdot), h(\cdot)$	Real even windows.
$s_r(m)$	Discrete azimuth signal.
f_n	Doppler frequency bin.
s_h	Sharpness value.
$\psi(\cdot)$	Convex function.
W_{sh}	Length of sliding window in sharpness analysis.
m_{opt}^b	Optimal start imaging moment.
m_{opt}^e	Optimal end imaging moment.
T_w^{opt}	Optimal time window.
L_{opt}	Optimal time window length.
\mathbf{M}_n	Search region for optimal start or end moment.
$E(I)$	Image entropy.
$I(m, n)$	ISAR image.

I. INTRODUCTION

INVERSE synthetic aperture radar (ISAR) imaging of ship target has aroused widespread concern, especially in the field of marine supervision and control [1]–[6]. After ISAR imaging, the ship image will be applied for the target classification and recognition [7]–[12]. For this purpose, an appropriate ship ISAR image should have the essential features of presenting the ship’s single view, i.e., top or side view, high quality, and high resolution. Since the ship ISAR image obtained with the entire echo is usually defocused and hybrid-view, the selection of an optimal time window is very important [7], [13]–[16].

The view that the radar image shows is depended on the IPP. Hence, the IPP selection is the key to achieve the radar image with the ship’s top or side view. The image quality is related to the stationarity of Doppler frequency, and the azimuth resolution is decided by the relative rotation angle. Therefore, the Doppler

frequency analysis technique can be applied for selection [12], [17].

Generally, selecting an optimal time window can bring the following advantages. First, the ISAR image with ship’s side or top view can be generated [12], [17]. Second, the echo data with the optimal time window has smaller data size compared with the whole data, and the computational complexity can be decreased. Third, the echo data with the optimal time window can be processed efficiently via the simple imaging techniques, such as RD algorithm, because the Doppler frequency is relatively stable in a short time window [17]–[21]. For achieving the aforementioned advantages, the following functions should be considered:

- 1) IPP selection for single view;
- 2) the smooth Doppler frequency curve for high image quality; and
- 3) long TWL for high resolution.

Recently, research works on the time window selection for the ship ISAR imaging are abundant. Basically, they can be divided into two classes, which are focused on the selection of TWL or IPP, separately. The first kind of methods can obtain the optimal time window with the estimation of Doppler frequency. For acquiring the high image quality, the time window with the stable Doppler frequency is selected. In [22], Martorella and Berizzi propose a time window selection method based on the maximum contrast, which implements an iterative idea. Furthermore, many approaches based on the TFD and Doppler frequency estimation are presented in [23]–[27]. These approaches utilize the character that the Doppler frequency curve can reflect the stability of target motion [28]. Without the determination of IPP, these methods usually generate the ship ISAR image with hybrid view, which is inappropriate for target recognition.

The second kind of methods can obtain the optimal time window based on the IPP selection. Via the rotation parameters estimation, the time window with the dominant rotation direction can be found [12], [17], [29]. With the selection of IPP, the generated ISAR image can give the top or side view of ship. However, the azimuth resolution of ISAR image is comparatively low without the analysis of Doppler frequency, which is unfavorable for the target recognition as well.

In this article, we propose an OTWD approach based on the Doppler frequency analysis and IPP selection. The proposed approach takes into account the advantages of the two classes of methods, which can determine the optimal time window to generate the high-quality ISAR image with the top view or side view of ship target. Two main procedures of the proposed method are illustrated as follows. First, the “rough” time window is determined via the IPP selection approach in [30]; second, the optimal time window is achieved via the extended subdata generation, TFD calculation, Doppler frequency estimation and sharpness analysis.

In some situations, it is difficult to find the range bin with single scatterer to calculate TFD and estimate the Doppler frequency. For addressing this issue, a novel TFD extraction approach based on the clustering analysis is proposed, which can extract the TFD of single scatterer from the TFD of multiple scatterer.

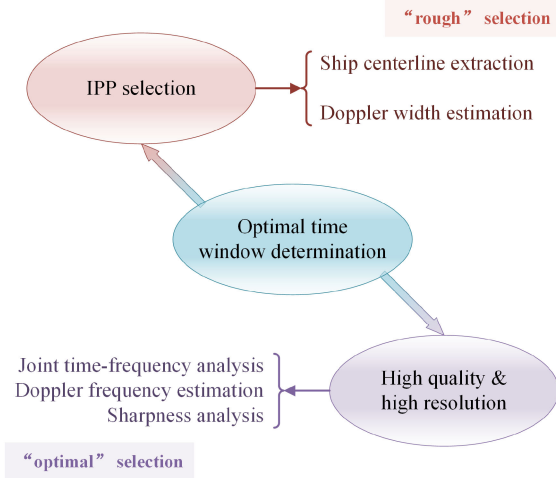


Fig. 1. Main work of this article.

The main work of this article can be seen in Fig. 1. The rest of the article is arranged as follows. In Section II, the ISAR imaging geometry is modeled, the IPP selection principle is deduced, and the IPP selection method is introduced. Then, the influence of TWL is analyzed for the image quality and azimuth resolution in Section III. Meanwhile, the OTWD approach is proposed based on the Doppler frequency analysis and IPP selection. For the situation of a certain range bin with multiple scatterers, the TFD extraction approach based on the clustering analysis is presented. For verification, results of simulated and real-measured data are given and analyzed in Section IV. Finally, we draw the conclusion of this article in Section V.

II. ISAR IMAGING GEOMETRY MODEL, IPP SELECTION PRINCIPLE, AND IPP SELECTION APPROACH

Some contents are introduced in this section including the ISAR imaging geometry model, the relationship between IPP and rotation vectors, the IPP selection principle and approach. First, the ISAR imaging geometry is modeled to solve the position of scatterer. Then, we deduce the expression of rotation vectors and illustrate the relationship between IPP and rotation vectors. Furthermore, the IPP selection principle is concluded. Finally, the IPP selection approach is introduced based on [30].

A. ISAR Imaging Geometry Model

The ship target can be regarded as a rotation target after translation compensation [31], [32]. The grazing angle can be considered as small, because the radar height is usually much less than the range between the radar and target. Hence, we assume that the radar height can be ignored. Fig. 2 shows the ISAR imaging geometry model. We denote the centroid of ship as O and two coordinate systems are established as follows:

- 1) Ship coordinate system O-RPY: R -axis is parallel to the ship's bow and Y is perpendicular to the sea surface.
- 2) Radar coordinate system O-UVW: U -axis is parallel to the direction of RLOS and W -axis is the same as Y -axis.

Obviously, the O-RPY and O-UVW can be transformed via rotation operation. Assuming that a scatterer A is on the ship target, the coordinate of scatterer A in O-RPY is as follows:

$$\mathbf{r} = [r_A, p_A, \eta_A]^T \quad (1)$$

where r_A, p_A, η_A are the coordinates of axis $R, P,$ and Y .

The ship target is rotating around the axis $R, P,$ and Y . In the imaging interval, the three-dimensional (3-D) (roll, pitch, and yaw) rotation angles are denoted as $\theta_r, \theta_p,$ and $\theta_y,$ respectively. Then, the instantaneous position of scatterer A in O-RPY can be calculated as follows:

$$\tilde{\mathbf{r}}(t_m) = [\tilde{r}_A(t_m), \tilde{p}_A(t_m), \tilde{\eta}_A(t_m)]^T = \mathbf{R}_r(\theta_r, \theta_p, \theta_y) \cdot \mathbf{r} \quad (2)$$

where t_m is the slow time, \mathbf{R}_r represents the 3-D rotation matrix, and $\tilde{r}_A(t_m), \tilde{p}_A(t_m), \tilde{\eta}_A(t_m)$ are instantaneous coordinates of axis $R, P,$ and $Y,$ respectively. The rotation matrix \mathbf{R}_r can be obtained as follows:

$$\mathbf{R}_r(\theta_r, \theta_p, \theta_y) = \mathbf{R}_{\text{roll}}(\theta_r) \cdot \mathbf{R}_{\text{pitch}}(\theta_p) \cdot \mathbf{R}_{\text{yaw}}(\theta_y) \quad (3)$$

$$\mathbf{R}_{\text{roll}}(\theta_r) = \begin{bmatrix} 1 & 0 & 0 \\ 0 & \cos \theta_r & \sin \theta_r \\ 0 & -\sin \theta_r & \cos \theta_r \end{bmatrix} \quad (4)$$

$$\mathbf{R}_{\text{pitch}}(\theta_p) = \begin{bmatrix} \cos \theta_p & 0 & \sin \theta_p \\ 0 & 1 & 0 \\ -\sin \theta_p & 0 & \cos \theta_p \end{bmatrix} \quad (5)$$

$$\mathbf{R}_{\text{yaw}}(\theta_y) = \begin{bmatrix} \cos \theta_y & \sin \theta_y & 0 \\ -\sin \theta_y & \cos \theta_y & 0 \\ 0 & 0 & 1 \end{bmatrix} \quad (6)$$

where $\mathbf{R}_{\text{roll}}(\theta_r), \mathbf{R}_{\text{pitch}}(\theta_p),$ and $\mathbf{R}_{\text{yaw}}(\theta_y)$ represent the roll, pitch, and yaw rotation matrix, respectively.

Finally, the instantaneous coordinate in O-UVW can be given as follows:

$$\mathbf{u}(t_m) = [u_A(t_m), v_A(t_m), w_A(t_m)]^T = \mathbf{R}_T(\varphi_u) \cdot \tilde{\mathbf{r}}(t_m) \quad (7)$$

where $\mathbf{R}_T(\varphi_u)$ is the transform matrix. The expression of $\mathbf{R}_T(\varphi_u)$ can be shown as follows:

$$\mathbf{R}_T(\varphi_u) = \begin{bmatrix} \cos \varphi_u & -\sin \varphi_u & 0 \\ \sin \varphi_u & \cos \varphi_u & 0 \\ 0 & 0 & 1 \end{bmatrix} \quad (8)$$

where φ_u is the angle between axis R and U .

B. Relation Between IPP and Rotation Vector

After translation compensation, the azimuth signal of scatterer A can be modeled as follows:

$$s_r(t_m) = a_a(t_m) \exp \left[-j \frac{4\pi}{\lambda} R_A(t_m) \right] \quad (9)$$

where $a_a(\cdot)$ is the amplitude function in the azimuth direction, λ represents the wavelength, and $R_A(t_m)$ is the range between scatterer A and radar.

Actually, the range of $R_A(t_m)$ in (9) can be calculated as follows:

$$R_A(t_m) = u_A(t_m) - u_r \quad (10)$$

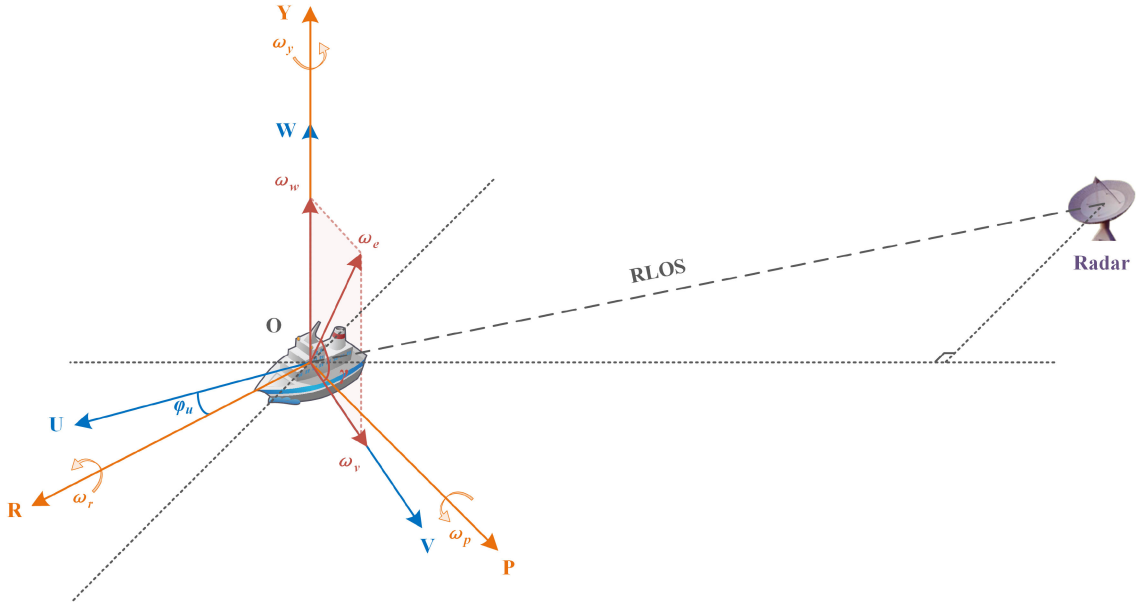


Fig. 2. ISAR imaging geometry.

where $u_A(t_m)$ and $-u_r$ are the U -axis coordinates of scatterer A and radar, respectively.

The coordinate $u_A(t_m)$ can be calculated via (7). Here, we introduce another calculation method. For the ship target without rotation motion, the coordinate of scatterer A in O-UVW coordinate is as follows:

$$\mathbf{u}_0 = [u_{A0}, v_{A0}, w_{A0}]^T = \mathbf{R}_T(\varphi_u) \cdot \mathbf{r}. \quad (11)$$

Then, for the ship target with 3-D rotation, we can rewrite (7) as follows:

$$\mathbf{u}(t_m) = \mathbf{R}_r(\theta_u, \theta_v, \theta_w) \cdot \mathbf{u}_0 \quad (12)$$

where the form of $\mathbf{R}_r(\theta_u, \theta_v, \theta_w)$ is the same as (3).

The rotation angles θ_u, θ_v , and θ_w can be integrated as follows:

$$\theta_u = \int_{T_w} \omega_u(t_m) dt_m \quad (13)$$

$$\theta_v = \int_{T_w} \omega_v(t_m) dt_m \quad (14)$$

$$\theta_w = \int_{T_w} \omega_w(t_m) dt_m \quad (15)$$

where T_w is the time window and $\omega_u, \omega_v, \omega_w$ are the angular speeds around the axis U, V , and W .

With the selection of time window, the TWL will be short and the motion of ship target can be considered as stable. Hence, the angular velocities $\omega_u(t_m)$, $\omega_v(t_m)$, and $\omega_w(t_m)$ can be regarded as constants. Apparently, these angular velocities can be transformed as follows:

$$\begin{bmatrix} \omega_u \\ \omega_v \\ \omega_w \end{bmatrix} = \mathbf{R}_T(\varphi_u) \cdot \begin{bmatrix} \omega_r \\ \omega_p \\ \omega_y \end{bmatrix}. \quad (16)$$

Hence, the horizontal and vertical effective rotation angular velocities are as follows:

$$\omega_v = \omega_r \sin \varphi_u + \omega_p \cos \varphi_u \quad (17)$$

$$\omega_w = \omega_y. \quad (18)$$

From (17) and (18), we can see that the horizontal rotation is related to the roll and pitch rotation, while the vertical rotation is depended on the yaw rotation.

Based on (17) and (18), we can obtain the effective rotation angular velocity as follows:

$$\omega_e = \sqrt{\omega_v^2 + \omega_w^2}. \quad (19)$$

According to Fig. 2, the horizontal and vertical rotations in (17) and (18) can also be rewritten as follows:

$$\omega_v = \omega_e \cos \gamma \quad (20)$$

$$\omega_w = \omega_e \sin \gamma \quad (21)$$

where γ is the angle between the vector ω_e and ω_v .

The derivation about the effective rotation speed can be verified with the projection principle. Actually, the effective rotation vector ω_e is produced via the projecting synthesis rotation vector ω_a onto the plane VOW. The plane VOW is the projection plane. The 3-D rotation vector in O-RPY can be expressed as follows:

$$\omega_r = [\omega_r, 0, 0]^T \quad (22)$$

$$\omega_p = [0, \omega_p, 0]^T \quad (23)$$

$$\omega_y = [0, 0, \omega_y]^T. \quad (24)$$

Then, the synthesis rotation vector can be calculated as follows:

$$\begin{aligned} \omega_a &= \omega_r + \omega_p + \omega_y \\ &= [\omega_r, \omega_p, \omega_y]^T. \end{aligned} \quad (25)$$

The normal vector of plane VOW in O-UVW can be expressed as $\mathbf{m} = [1, 0, 0]^T$. With the coordinate transformation, the normal vector in O-RPY can be calculated as follows:

$$\begin{aligned}\tilde{\mathbf{m}} &= (\mathbf{R}_T(\varphi_u))^{-1} \cdot \mathbf{m} \\ &= [\cos \varphi_u, -\sin \varphi_u, 0]^T.\end{aligned}\quad (26)$$

Then, the angle between the plane VOW and synthesis rotation vector can be solved as follows:

$$\begin{aligned}\beta &= \arcsin\left(\frac{\boldsymbol{\omega}_a \cdot \tilde{\mathbf{m}}}{\|\boldsymbol{\omega}_a\|_2 \|\tilde{\mathbf{m}}\|_2}\right) \\ &= \arcsin\left(\frac{\omega_r \cos \varphi_u - \omega_p \sin \varphi_u}{\|\boldsymbol{\omega}_a\|_2}\right).\end{aligned}\quad (27)$$

The effective rotation vector is the projection of synthesis rotation vector with the angle β . The effective rotation vector in O-RPY can be calculated as follows:

$$\begin{aligned}\boldsymbol{\omega}_e^{\text{RPY}} &= \boldsymbol{\omega}_a - (\boldsymbol{\omega}_a \cdot \tilde{\mathbf{m}}) \cdot \tilde{\mathbf{m}} \\ &= \begin{bmatrix} \omega_r \sin^2 \varphi_u + \omega_p \sin \varphi_u \cos \varphi_u \\ \omega_p \cos^2 \varphi_u + \omega_r \sin \varphi_u \cos \varphi_u \\ \omega_y \end{bmatrix}.\end{aligned}\quad (28)$$

According to (7), the effective rotation vector in O-UVW can be obtained as follows:

$$\begin{aligned}\boldsymbol{\omega}_e &= [\omega_u, \omega_v, \omega_w]^T \\ &= \mathbf{R}_T(\varphi_u) \boldsymbol{\omega}_e^{\text{RPY}} \\ &= [0, \omega_r \sin \varphi_u + \omega_p \cos \varphi_u, \omega_y]^T\end{aligned}\quad (29)$$

which is conformed to (17) and (18).

The norm of vector $\boldsymbol{\omega}_e$ can be calculated as follows:

$$\begin{aligned}\|\boldsymbol{\omega}_e\|_2 &= \|\boldsymbol{\omega}_a\|_2 \cos \beta \\ &= (\omega_r \sin \varphi_u + \omega_p \cos \varphi_u)^2 + \omega_y^2.\end{aligned}\quad (30)$$

Fig. 3 gives the IPPs under different rotation conditions. Fig. 3(a) and (b) show conditions of the prominent vertical rotation and prominent horizontal rotation. The case that horizontal and vertical rotation are almost equal is displayed in Fig. 3(c).

As well known, the IPP is perpendicular to the effective rotation vector and parallel to RLOS. Therefore, from (17) to (19), three conclusions can be drawn as follows.

- 1) When the horizontal rotation is far smaller than vertical rotation, i.e., $\omega_w \approx \omega_e$ and $\omega_v \approx 0$, we will gain a ISAR image with the ship's top view as shown in Fig. 3(a).
- 2) When the horizontal rotation is far bigger than vertical rotation, i.e., $\omega_w = 0$ and $\omega_v \approx \omega_e$, we will obtain a ISAR image with the ship's side view as shown in Fig. 3(b).
- 3) Otherwise, we will generate a ISAR image with the ship's hybrid view as shown in Fig. 3(c).

Remark 1: In this article, the IPP selection is as the first core step in the proposed OTWD approach. The radar image with the side view or top view of ship target is generated via the IPP selection, which is demanded by some algorithms of target feature extraction, classification, and recognition. Actually, the radar image with the hybrid view of ship target can reach the same or even higher image quality, while it will reduce the

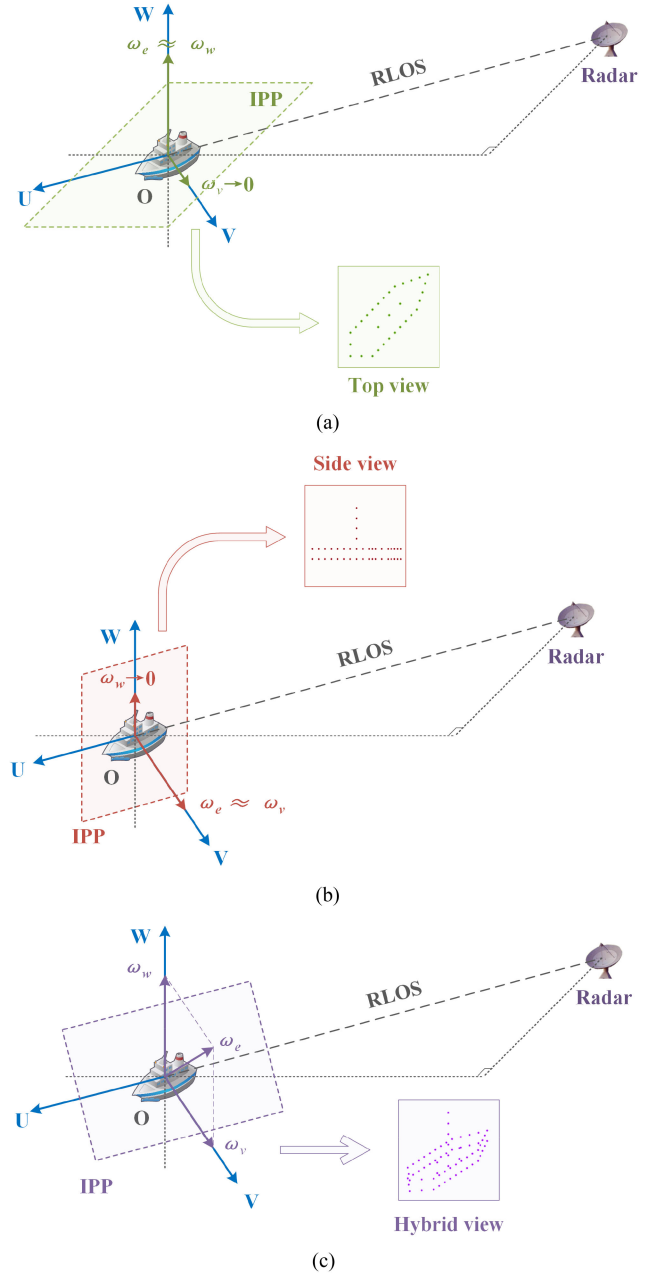


Fig. 3. IPPs under different rotation conditions. (a) Prominent vertical rotation. (b) Prominent horizontal rotation. (c) Almost equal horizontal and vertical rotation.

recognition efficiency and accuracy. Hence, the IPP selection is implemented first in the proposed approach.

C. IPP Selection Principle

In a short TWL, the rotation angles θ_u , θ_v , and θ_w are small and the angle velocities can be regarded as constants. Hence, the functions of $\sin \theta_j$ and $\cos \theta_j$ can be approximated as follows:

$$\sin \theta_j \approx \theta_j, j = u, v, w \quad (31)$$

$$\cos \theta_j = 1, j = u, v, w \quad (32)$$

where j represents the direction of axis U , V , or W . Here, $\omega_j(t_m)$ can be denoted as ω_j , $j = u, v, w$.

Then, the expression of $\mathbf{R}_r(\theta_u, \theta_v, \theta_w)$ can be rewritten as follows:

$$\mathbf{R}_r(\theta_u, \theta_v, \theta_w) = \begin{bmatrix} 1 & \theta_w & \theta_v \\ -\theta_u\theta_v - \theta_w & -\theta_u\theta_v\theta_w + 1 & \theta_u \\ -\theta_v + \theta_u\theta_w & -\theta_v\theta_w - \theta_u & 1 \end{bmatrix}. \quad (33)$$

Based on (12), the range $u_A(t_m)$ can be expressed as follows:

$$u_A(t_m) = u_{A0} + v_{A0}\theta_w + w_{A0}\theta_v. \quad (34)$$

Therefore, the range $R_A(t_m)$ can be represented as follows:

$$\begin{aligned} R_A(t_m) &= v_{A0}\theta_w + w_{A0}\theta_v + (u_{A0} - u_r) \\ &= (v_{A0}\omega_w + w_{A0}\omega_v)t_m + (u_{A0} - u_r). \end{aligned} \quad (35)$$

In (35), the range $R_A(t_m)$ is modeled as the first-order polynomial of t_m .

The Doppler frequency can be calculated as follows:

$$f_d^A = -\frac{2}{\lambda} \frac{dR(t_m)}{dt_m} = -\frac{2}{\lambda} (v_{A0}\omega_w + w_{A0}\omega_v). \quad (36)$$

According to (20) and (21), the Doppler frequency in (36) can be rewritten as follows:

$$f_d^A = -\frac{2}{\lambda} (v_{A0} \sin \gamma + w_{A0} \cos \gamma) \omega_e. \quad (37)$$

Based on (37), the Doppler frequency is a constant. Hence, the ship ISAR image with a short time window will not be blurred in the azimuth direction.

Assuming that two scatterers A_b and A_s are located in the bow and stern [12], [17], and their coordinates in O-RPY are $[r_{Ab}, 0, w_{A0}]^T$ and $[r_{As}, 0, w_{A0}]^T$, respectively. Transforming via (11), the coordinates can be represented as follows:

$$\mathbf{u}_{Ab} = [u_{Ab}, v_{Ab}, w_{Ab}]^T = [r_{Ab} \cos \varphi_u, r_{Ab} \sin \varphi_u, w_{A0}]^T \quad (38)$$

$$\mathbf{u}_{As} = [u_{As}, v_{As}, w_{As}]^T = [r_{As} \cos \varphi_u, r_{As} \sin \varphi_u, w_{A0}]^T. \quad (39)$$

Via (37), the Doppler frequency of the scatterer A_b and A_s can be calculated as follows:

$$\begin{aligned} f_d^{Ab} &= -\frac{2}{\lambda} [v_{Ab} \sin \gamma + w_{A0} \cos \gamma] \omega_e \\ &= -\frac{2}{\lambda} [r_{Ab} \sin \varphi_u \sin \gamma + w_{A0} \cos \gamma] \omega_e \end{aligned} \quad (40)$$

$$\begin{aligned} f_d^{As} &= -\frac{2}{\lambda} [v_{As} \sin \gamma + w_{A0} \cos \gamma] \omega_e \\ &= -\frac{2}{\lambda} [r_{As} \sin \varphi_u \sin \gamma + w_{A0} \cos \gamma] \omega_e. \end{aligned} \quad (41)$$

Then, the difference of Doppler frequency can be computed with (40) and (41) as follows:

$$f_d^\Delta = f_d^{Ab}(t_m) - f_d^{As}(t_m) = \frac{2}{\lambda} (r_{As} - r_{Ab}) \sin \varphi_u \omega_w. \quad (42)$$

Meanwhile, the range difference of the scatterer A_b and A_s can be obtained as well. From (38) and (39), the range difference

can be shown as follows:

$$u_\Delta = u_{Ab} - u_{As} = (r_{Ab} - r_{As}) \cos \varphi_u. \quad (43)$$

Combining with (42) and (43), the slope value of ship centerline can be calculated as follows:

$$k_s = \frac{f_d^\Delta}{u_{A\Delta}} = -\frac{2}{\lambda} \tan \varphi_u \omega_w. \quad (44)$$

Obviously, the vertical rotation is related with the slope value of ship centerline.

The variation of effective rotation speed ω_e can be depicted by the Doppler spread in the ISAR image. First, we illustrate this relationship from the point of azimuth resolution. The greater effective rotation speed will yield the larger rotation angle with the same TWL. Consequently, the azimuth resolution will be enhanced. The high resolution will make the ship target occupying more azimuth bin in the ISAR image, i.e., larger Doppler spread. Hence, the effective rotation can be reflected by the Doppler spread.

Furthermore, the relationship between the effective rotation and Doppler spread can be elaborated with the analysis of azimuth position. The effective rotation vector and the unit vector in the direction of RLOS can be expressed as follows:

$$\boldsymbol{\omega}_e = [0, \omega_r \sin \varphi_u + \omega_p \cos \varphi_u, \omega_y]^T \quad (45)$$

$$\mathbf{u}_u^1 = [1, 0, 0]^T. \quad (46)$$

The Doppler frequency can be produced with the angular moment that is same with the azimuth direction in (37). The normal vector of this angular moment is as follows:

$$\tilde{\mathbf{n}} = [0, \sin \gamma, \cos \gamma]^T. \quad (47)$$

The azimuth position can be calculated via projecting the scatterer coordinate into the direction $\tilde{\mathbf{n}}$, which can be calculated as follows:

$$\begin{aligned} x_a &= \mathbf{u}_0 \cdot \tilde{\mathbf{n}} \\ &= v_{A0} \sin \gamma + w_{A0} \cos \gamma. \end{aligned} \quad (48)$$

For one ship target, the difference of azimuth position can be represented as follows:

$$\Delta x_a = \Delta v_{A0} \sin \gamma + \Delta w_{A0} \cos \gamma \quad (49)$$

where Δv_{A0} and Δw_{A0} are the differences of ship target in the axis V and W , respectively.

Then, the Doppler spread can be solved as follows:

$$\begin{aligned} \Delta f_d &= \frac{2\omega_e \Delta x_a}{\lambda} \\ &= \frac{2}{\lambda} (\Delta v_{A0} \sin \gamma + \Delta w_{A0} \cos \gamma) \omega_e \end{aligned} \quad (50)$$

where the value of $\Delta v_{A0} \sin \gamma + \Delta w_{A0} \cos \gamma$ in the ship target is determined. Hence, the Doppler spread is related with the effective rotation and IPP.

In this article, we adopt the IPP selection principle proposed by Pastina to determine the time interval which can produce the ISAR image with the ship's top view or side view [12], [17]. When the curves of absolute ship's centerline slope and Doppler

TABLE I
IPP SELECTION PRINCIPLE

Trend of curves about centerline slope and Doppler spread	Absolute slope value of ship centerline	Doppler spread	IPP or ISAR image
Synchronously	Larger	Smaller	Top view
Arbitrarily	Smaller	Larger	Side view
Arbitrarily	Otherwise	Otherwise	Hybrid view

spread own the synchronous trend that is increasing and reaching to the maximum and then decreasing, the horizontal rotation is considered as weak and the vertical rotation is dominant. Then, the time interval characterized by larger slope value and smaller Doppler spread is selected for yielding the ship image with top view. When the slope of ship's centerline is closed to zero, the vertical rotation is regarded as weak and the horizontal rotation is dominant. Afterward, the time interval which has nearly slope rate of zero and larger Doppler spread can be chosen for generating the ship image with side view. The IPP selection principle in [12] and [17] is summarized as Table I.

Remark 2: It is worth noting that the curves of ship centerline slope and Doppler spread can have synchronous trend as well when the horizontal and vertical rotation vary similarly. Under this circumstance, the IPP principle cannot distinguish the dominant rotation direction well, especially when the horizontal rotation amplitude is closed to the vertical rotation amplitude. Fortunately, this phenomenon will rarely happen to the ship target on the sea surface, because the ship target generally rotates around a dominant direction in the short time window. Hence, the dominant rotation direction can be distinguished via the IPP principle in Table I.

D. IPP Selection Method

When the vertical rotation is dominant, the radar image with ship's top view can be generated as shown in Fig. 3(a). When the horizontal rotation is dominant, the radar image with ship's side view can be obtained as shown in Fig. 3(b). When the horizontal and vertical rotation is almost equal, we can attain the radar image with ship's hybrid view as seen in Fig. 3(c). For better target classification and recognition, the radar image with the top view or side view of ship target need to be generated. For this purpose, the time window which has the dominantly horizontal or vertical rotation need to be obtained. The variation trend of vertical rotation can be obtained via the estimation of ship's centerline slope based on (44). However, the change of horizontal rotation is difficult to obtain. Here, we indirectly estimate the change of horizontal rotation via the effective rotation estimation. The variation trend of effective rotation can be estimated with the Doppler spread based on (50).

In this article, we apply the ship centerline extraction approach in [30] to estimate the slope value. Meanwhile, the azimuth numbers for the Doppler spread are measured via the ship ISAR image.

Before the parameter estimation, the entire echo data needs to be divided into some subdata along the azimuth direction. We apply a sliding window to generate the subdata. The echo

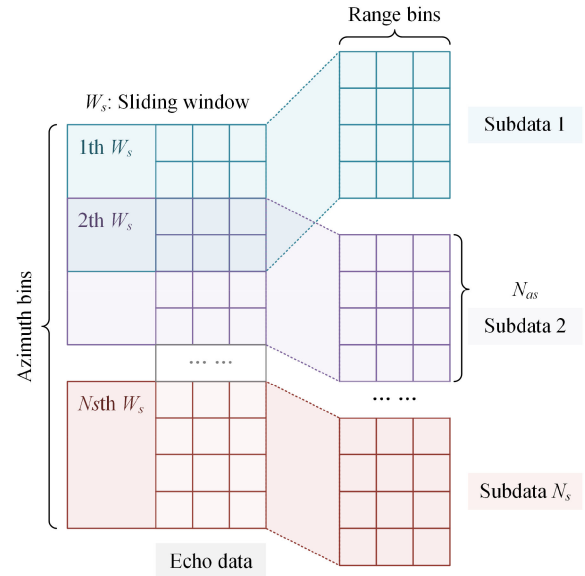


Fig. 4. Flowchart of subdata generation via sliding window.

data is denoted as $s_r(m, n)$, where m and n are the orders of azimuth and range bins, respectively. Meanwhile, the 2-D sizes of echo are N_a and N_r . The subdata sequence can be expressed as follows:

$$s_r^q(m, n) = s_r(m_s, n),$$

$$m_s \in [1 + (q - 1)N_{as}/2, N_{as} + (q - 1)N_{as}/2] \quad (51)$$

where $s_r^q(m, n)$ represents the q th subdata, m_s is the azimuth scope of subdata in $s_r(m, n)$, and N_{as} is an even number which represents the sliding window width in azimuth. This procedure can be seen in Fig. 4.

The selection of IPP is based on the division of subaperture and the estimation of rotation parameters. The division of subaperture will influence the estimation precision and computing time of rotation parameters. Too small azimuth size of subaperture will reduce the estimated precision. However, too large azimuth size will lose details of estimation curves and increase the computing time. Hence, the azimuth size should be selected properly. Selection standards for the azimuth size of subdata will be elaborated in Section IV.

The ship centerline extraction approach in [30] utilizes the line group and Hough transform to measure the ship width and the centerline slope. The core function is shown in the following equation:

$$F(\rho_w, \rho_0, \theta) = \sum_{\rho} C(\rho, \theta) \quad (52)$$

where ρ , ρ_w , and ρ_0 are polar radius, accumulation width, and initial polar radius, accumulating function $C(\rho, \theta)$ represents the sum of image pixel on the line (ρ, θ) , and θ represents the direction of accumulation.

The accurate accumulating width and direction can be searched as follows: When the optimal ship width is obtained, the core function will change sharply with the accumulating

direction. When the optimal ship width is not acquired, the core function will change mildly with the accumulating direction.

The main procedures of ship centerline extraction method are listed in [30].

- 1) Implement the subdata generation, translation compensation, and RD imaging.
- 2) The matrix \mathbf{H}_0 is obtained by Hough transform.
- 3) Accumulating the matrix \mathbf{H}_0 with the width ρ_w , the matrix \mathbf{H}_w is obtained.
- 4) After extracting the N_w maximums of \mathbf{H}_w , the maximum sequence can be formed and the variance of the sequence can be calculated.
- 5) Repeating the steps 3) and 4), the variance sequence can be consisted.
- 6) Searching the maximum of the variance sequence, the corresponding optimal accumulation width $\hat{\rho}_w$ can be acquired.
- 7) Calculating the matrix \mathbf{H}_w with the width $\hat{\rho}_w$, the optimal accumulating direction $\hat{\theta}$ can be generated and the slope of ship centerline can be calculated as $\hat{k}_s = \tan \hat{\theta}$.

The azimuth numbers for the Doppler spread can be calculated via measuring the azimuth scope of ship target in the ISAR image. The maximum and minimum azimuth bins are denoted as D_{\max} and D_{\min} , respectively. Then, the azimuth numbers for the Doppler spread can be calculated as follows:

$$D_w = D_{\max} - D_{\min}. \quad (53)$$

The flowchart of the IPP estimation approach is shown in Fig. 5.

III. OPTIMAL TIME WINDOW DETERMINATION APPROACH

For the echo data with long observation time, the ISAR image will be blurred and unrecognizable via the RD algorithm. After the time window selection, we can generate the well-focused ISAR image with RD algorithm. In this section, the OTWD approach is proposed based on the IPP selection and Doppler frequency analysis. The proposed OTWD approach includes rotation parameters estimation, extended subdata generation, TFD calculation, Doppler frequency estimation, and sharpness analysis. For the estimation of Doppler frequency estimation, the TFD of one scatterer is required. However, the range bin with one scatterer may not be found easily. For solving this problem, a novel TFD extraction approach based on the clustering algorithm is proposed in this article. The main flowchart of the proposed approach is shown in Fig. 6.

In this article, the “subdata,” “extended subdata,” and “optimal subdata” are defined as follows.

Definition 1: subdata. The expression of the subdata can be seen in (51). It refers to the subdata that is introduced in the Section II-D. The subdata is divided from the entire echo data and is utilized for the rotation parameter estimation and IPP selection.

Definition 2: extended subdata. The extended subdata is combined with three parts of the subdata. The expression of it can be represented as $s_r^E(m, n) =$

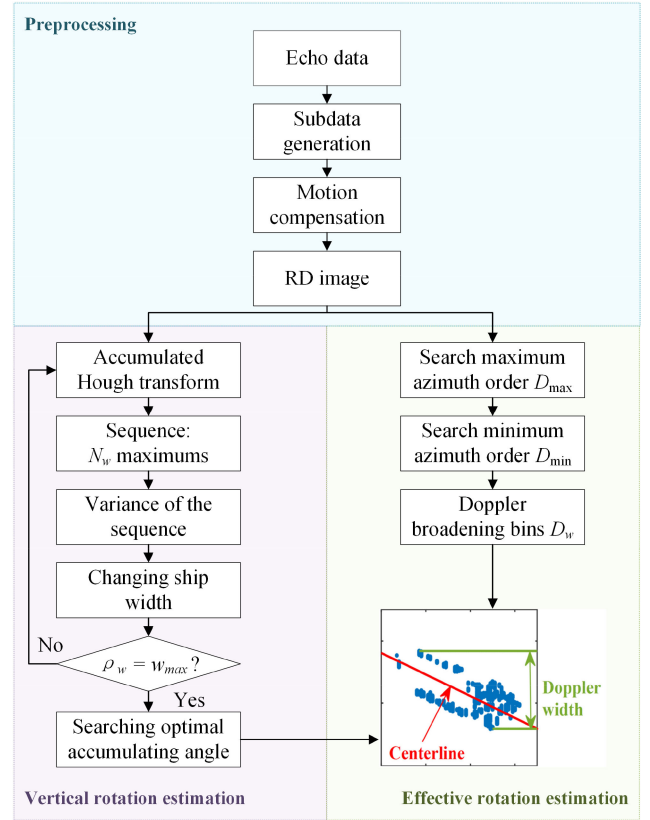


Fig. 5. Flowchart of IPP estimation approach.

$[s_r^{q-2}(m, n) \ s_r^q(m, n) \ s_r^{q+2}(m, n)]^T$. The generated extended subdata will be used for the Doppler frequency analysis.

Definition 3: optimal subdata. The optimal time window can be obtained via the OTWD approach. The echo data with the optimal time window is denoted as the optimal subdata.

The relationship among the subdata, extended subdata, and optimal subdata is shown in Fig. 7.

A. Analysis of Time Window

Section II-C and D introduce the IPP selection principle and approach. After IPP determination, the relatively appropriate time window can be selected “roughly.” However, the time window can be further optimized. Fig. 8 gives a part of change curves about the slope for the ship centerline and the azimuth numbers for the Doppler spread. The green area shows the time window determined via the IPP selection. In the green area, the absolute slope of ship centerline reaches the maximum value and the azimuth numbers for the Doppler spread is relatively small. Whereas, the curves almost have the same feature in the blue ellipse area. Hence, the optimal start and end imaging moment may appear earlier or later and the optimal TWL may be longer. The ship ISAR image can be improved from the quality and resolution via the time window selection.

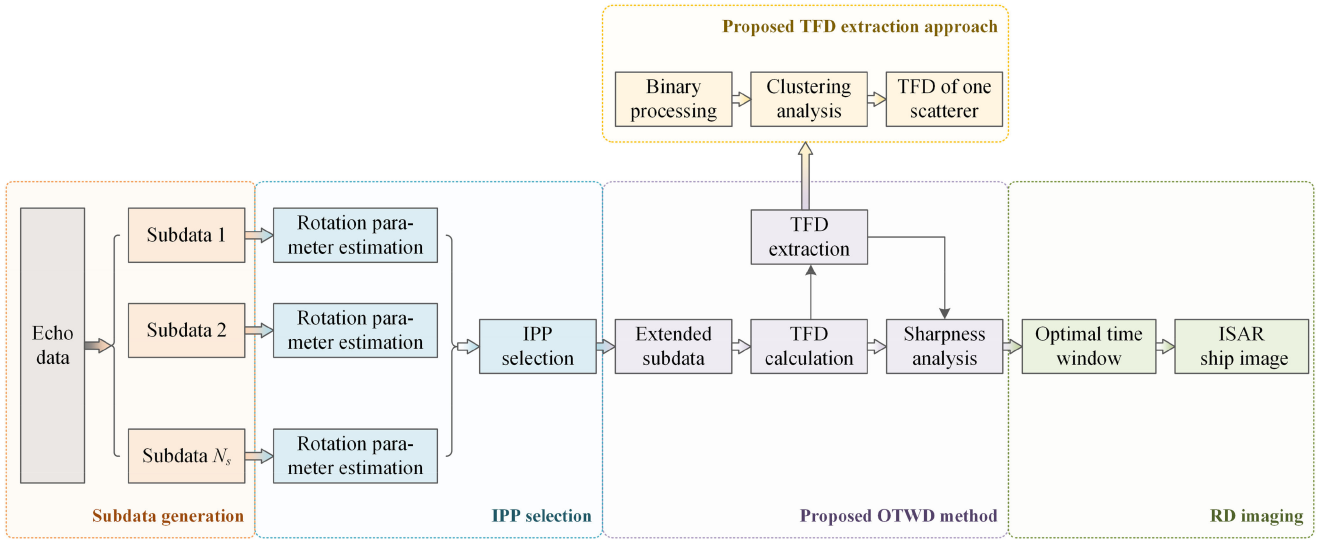


Fig. 6. Flowchart of the proposed OTWD based on IPP selection and Doppler frequency analysis.

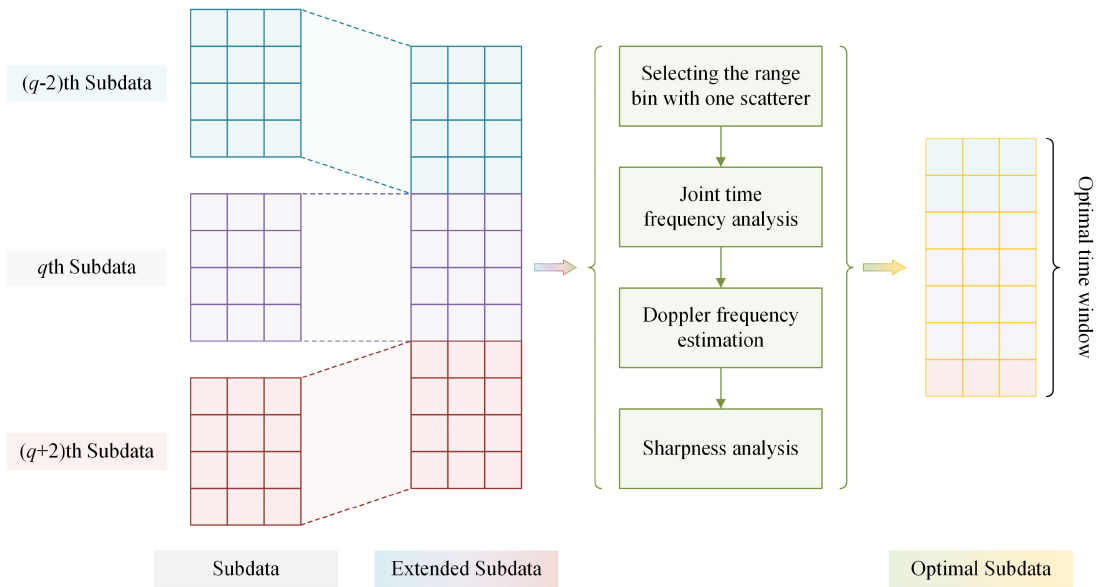


Fig. 7. Relationship among the subdata, extended subdata, and optimal subdata.

Under the low sea condition, the rotation vector will not change sharply. Hence, the optimal TWL will be longer than the TWL of subdata. Obtaining the optimal TWL, the azimuth resolution of ISAR image can be improved. The azimuth resolution can be expressed as follows:

$$\rho_a = \frac{\lambda}{2\Delta\theta} = \frac{\lambda}{2\omega_e T_w} \quad (54)$$

where $\Delta\theta$ is the rotation angle. Based on (54), we can see that enlarging the TWL is beneficial to the image resolution.

However, the TWL cannot be too long. In the short time window, the rotation vector is regarded as unchanged. Actually, the rotation angle can be modeled as sinusoidal rotation in the

following:

$$\theta_i(t_m) = \frac{A_i}{2} \sin\left(\frac{2\pi}{\tau_i} t_m + \phi_i\right), i = r, p, y \quad (55)$$

where A , τ , and ϕ represent the rotation amplitude, rotation period, and initial rotation phase, respectively.

According to (16)–(18), the rotation angular velocity in O-UUVW can be calculated as follows:

$$\omega_u(t_m) = \omega_r(t_m) \cos \varphi_u - \omega_p(t_m) \sin \varphi_u \quad (56)$$

$$\omega_v(t_m) = \omega_r(t_m) \sin \varphi_u + \omega_p(t_m) \cos \varphi_u \quad (57)$$

$$\omega_w(t_m) = \omega_y(t_m). \quad (58)$$

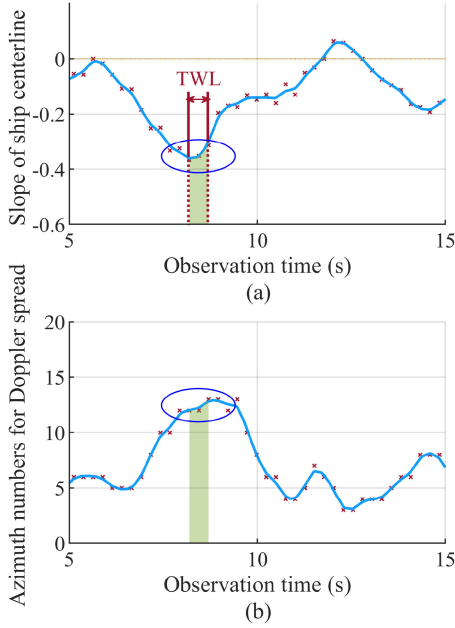


Fig. 8. Description of the optimal TWL. (a) Change curve of ship centerline slope. (b) Change curve of azimuth numbers for Doppler spread.

Then, based on (13)–(15), the rotation angles in O-UVW can be obtained as follows:

$$\theta_u(t_m) = \theta_r(t_m) \cos \varphi_u - \theta_p(t_m) \sin \varphi_u \quad (59)$$

$$\theta_v(t_m) = \theta_r(t_m) \sin \varphi_u + \theta_p(t_m) \cos \varphi_u \quad (60)$$

$$\theta_w(t_m) = \theta_y(t_m). \quad (61)$$

For simplification, we assume the angle $\varphi_u = 0$. The rotation angles in (59) and (60) can be rewritten as follows:

$$\theta_u(t_m) = \theta_r(t_m) \quad (62)$$

$$\theta_v(t_m) = \theta_p(t_m). \quad (63)$$

The functions $\sin(\theta_j(t_m))$ and $\cos(\theta_j(t_m))$ are as follows:

$$\sin(\theta_j(t_m)) = \sin(\theta_i(t_m)) \quad (64)$$

$$\cos(\theta_j(t_m)) = \cos(\theta_i(t_m)) \quad (65)$$

where $i = r, p, y$ and $j = u, v, w$. When the motion of ship target is not severe, the functions in (64) and (65) can be approximated as follows:

$$\sin(\theta_j(t_m)) \approx \frac{\pi A_i}{\tau_i} \left(t_m + \frac{\phi_i \tau_i}{2\pi} \right) \quad (66)$$

$$\cos(\theta_j(t_m)) \approx 1 - \frac{\pi^2 A_i^2}{2\tau_i^2} \left(t_m + \frac{\phi_i \tau_i}{2\pi} \right)^2. \quad (67)$$

The rotation matrix in O-UVW is as follows:

$$\begin{aligned} \mathbf{R}_r(\theta_u(t_m), \theta_v(t_m), \theta_w(t_m)) \\ = \mathbf{R}_r(\theta_r(t_m), \theta_p(t_m), \theta_y(t_m)) \end{aligned}$$

$$= \begin{bmatrix} \mu_{11}(t_m) & \mu_{12}(t_m) & \mu_{13}(t_m) \\ \mu_{21}(t_m) & \mu_{22}(t_m) & \mu_{23}(t_m) \\ \mu_{31}(t_m) & \mu_{32}(t_m) & \mu_{33}(t_m) \end{bmatrix}. \quad (68)$$

The parameters $\mu_{rc}(t_m)$ can be expressed as the second-order polynomial in the following:

$$\mu_{rc}(t_m) \approx \alpha_{rc}^2 t_m^2 + \alpha_{rc}^1 t_m + \alpha_{rc}^0 \quad (69)$$

where $r, c = 1, 2, 3$, α_{rc}^2 , α_{rc}^1 , and α_{rc}^0 are the second, the first, and the constant order of the polynomial.

According to (12), the U -axis coordinate of scatterer A can be calculated as follows:

$$u_A(t_m) = \mu_{11}(t_m) u_{A0} + \mu_{12}(t_m) v_{A0} + \mu_{13}(t_m) w_{A0} \quad (70)$$

Based on (10), (69), and (70), the range $R_A(t_m)$ can be approximated as follows:

$$R_A(t_m) = \rho_2 t_m^2 + \rho_1 t_m + \rho_0 \quad (71)$$

where ρ_2 , ρ_1 , and ρ_0 are the second, the first, and the constant order of the polynomial.

Afterwards, the Doppler frequency can be rewritten as follows:

$$f_d^A(t_m) = -\frac{2}{\lambda} \frac{dR_A(t_m)}{dt_m} = -\frac{2}{\lambda} (2\rho_2 t_m + \rho_1). \quad (72)$$

The Doppler frequency in (72) is varied with the slow time t_m , which will lead to the azimuth defocus. Under the high sea condition, the Doppler frequency can be modeled as the high-order polynomial. Hence, the quality of ISAR image will be reduced sharply with too long TWL.

Remark 3: Under the high sea condition, the approximation in (66) and (67) will be inappropriate owing to the sharp motion of ship target. The functions in (64) and (65) can be approximated as high-order polynomial. Accordingly, the Doppler frequency will vary with the slow time, which leads to the poor quality of ISAR image. Under the circumstance, the image quality can be ensured via the decrease of TWL. Owing to the fixed rotational direction, the rotational angle will be reduced with the decrease of TWL. Hence, compared with the ISAR image of subdata, the azimuth resolution of the image of optimal subdata will be slightly larger.

B. Proposed OTWD Approach

In this article, the OTWD approach is proposed based on the Doppler frequency analysis. The proposed method can determine the optimal time window, which has the almost invariant Doppler frequency. The flowchart of the proposed OTWD approach is shown in Fig. 9 and the main procedures are listed as follows:

- 1) The extended subdata is consisted with three parts of subdata in the following:

$$s_r^E(m, n) = \begin{bmatrix} s_r^{q-2}(m, n) \\ s_r^q(m, n) \\ s_r^{q+2}(m, n) \end{bmatrix}. \quad (73)$$

- 2) The range bin with the single scatterer is selected.

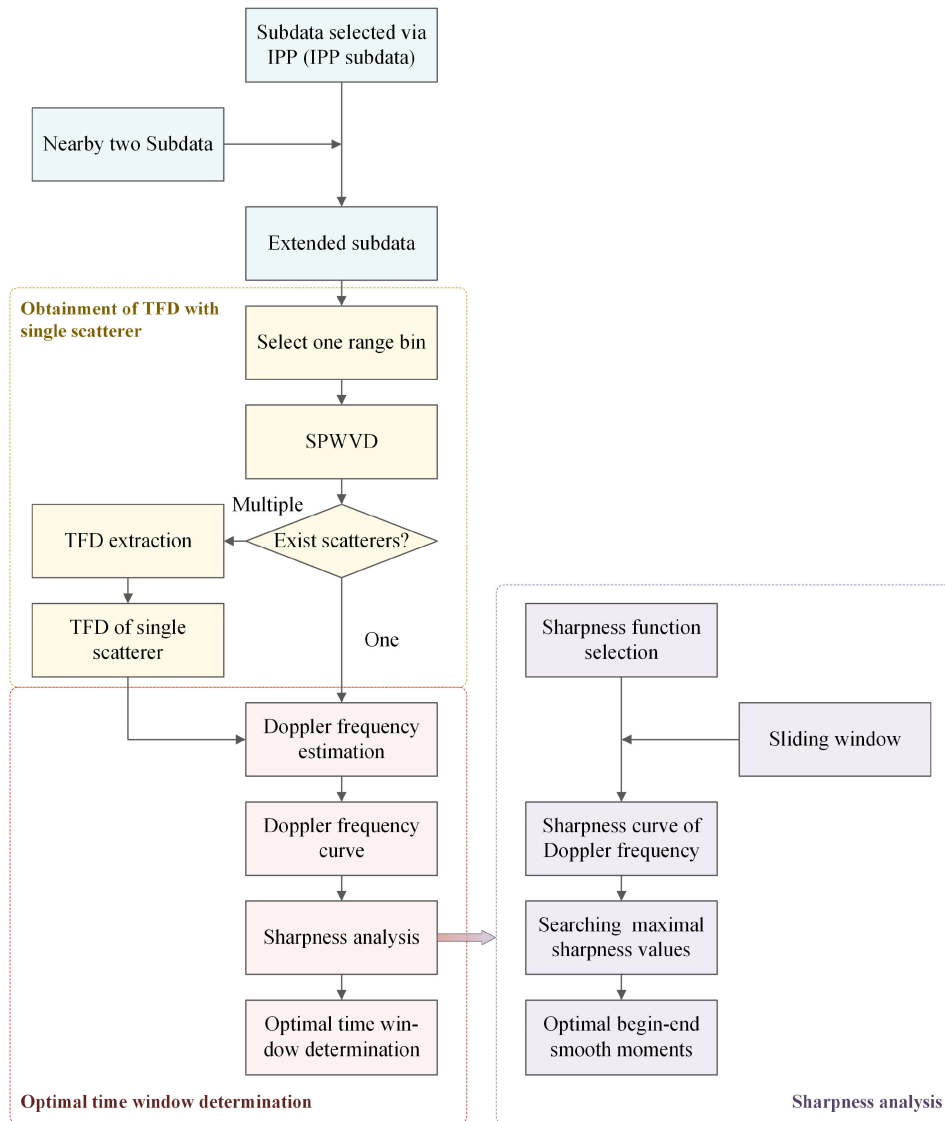


Fig. 9. Flowchart of the proposed OTWD approach.

- 3) The azimuth signal of this range bin is processed via the TFD calculation.
- 4) The Doppler frequency is estimated and the curve of the Doppler frequency can be generated.
- 5) The smoothness about the curve of Doppler frequency is measured via the sharpness analysis.
- 6) After selecting the start and end smooth moments, the optimal time window can be determined.

In step 1), three parts of subdata are combined as an extended subdata, because the start and end smooth moment may not exist in the “rough” time window selected by IPP.

In step 2), the range bin with one scatterer need to be selected. However, this kind of range bin may not be found in some potential situation, i.e., the TFD of one scatterer cannot be obtained. For the situation of multiple scatterers in a certain range bin, we propose a novel TFD extraction approach based on the clustering analysis. Fig. 10 gives the results of TFD extraction and shows the main procedures of the proposed approach as an example.

The main steps of the proposed approach are as follows. First, the TFD of one range bin with multiple scatterers are obtained as shown in Fig. 10(a). Second, the TFD result is binary processed with the OTSU method [33] as seen in Fig. 10(b). Third, the HCA is chosen for the classification of multiple scatterers’ TFD as shown in Fig. 10(c). Fourth, the binary TFD of one scatterer can be obtained as shown in Fig. 10(d). Then, the range of Doppler frequency in each observation moment can be determined. Combined with the TFD result in Fig. 10(a), the Doppler frequency can be estimated via searching the maximum value of $S(m, f_d)$. The Doppler frequency can be estimated as follows:

$$f_d(m) = \arg \max_{f_d \in \mathbf{F}_m} S(m, f_d) \quad (74)$$

$$\mathbf{F}_m = [f_{d_{\min}}^m, f_{d_{\max}}^m] \quad (75)$$

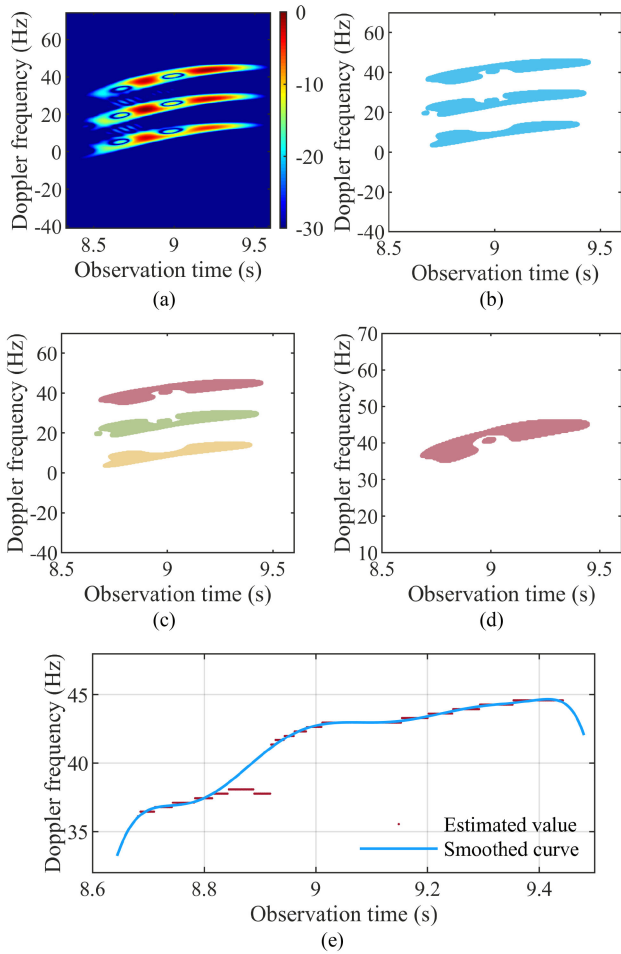


Fig. 10. Results of proposed TFD extraction approach based on the cluster analysis. (a) TFD result of one range bin with multiple scatterers. (b) Binaryzation result with OTSU method. (c) Clustering result via HCA. (d) Extraction result of binaryzation TFD. (e) Estimation result of Doppler frequency.

where $f_{d\min}^m$ and $f_{d\max}^m$ are the minimum and maximum Doppler frequency in the extracted binary TFD, respectively, and \mathbf{F}_m is the range of Doppler frequency.

Finally, the Doppler frequency of one scatterer can be estimated as shown in Fig. 10(e).

In step 3), the TFD we choose is the SPWVD, which can ensure the high time–frequency resolution and reduce cross-terms. The expression of SPWVD is shown in the following:

$$\begin{aligned}
 S(m, f_n) &= \int_{\tau} \int_u g(u) h(\tau) s_r \left(m - u + \frac{\tau}{2} \right) s_r^* \left(m - u - \frac{\tau}{2} \right) \\
 &\quad e^{-j2\pi f_n \tau} du d\tau \quad (76)
 \end{aligned}$$

where $g(u)$ and $h(\tau)$ are the real even windows, $s_r(m)$ and f_n represent the discrete azimuth signal and the Doppler frequency bin, respectively.

In step 4), the Doppler frequency can be estimated as follows:

$$f_d = \frac{\text{PRF}}{6N_{as}} f_n \quad (77)$$

where PRF is the pulse repetition frequency. The Doppler frequency curve is denoted as $f_d(m)$.

In step 5), the sharpness analysis method is proposed for searching the accurate start and end smooth moments. The definition of sharpness is given in [34] as follows:

$$s_h = \sum_m \psi \left(\frac{f_d(m)}{\chi} \right) \quad (78)$$

$$\chi = \sum_m f_d(m) \quad (79)$$

where s_h represents the sharpness of signal and $\psi(x)$ is a convex function. In this article, the convex function we apply is shown as follows:

$$\psi(x) = x \ln(x) \quad (80)$$

where x is between 0 and 1. The curve is more unsmooth with larger sharpness value.

The sharpness curve of Doppler frequency can be generated via the sharpness analysis. When the sharpness value reaches the maximal and is decreased, the curve will be regarded as starting smooth. Conversely, when the sharpness value is increased and reaches the maximal value, the curve will be considered as stopping smooth. The main procedures of the sharpness analysis are as follows.

- 1) The sharpness curve of the Doppler frequency is obtained via a sliding window as follows:

$$\begin{aligned}
 s_h(m) &= \sum_m \psi \left(\frac{f_d(m)}{\chi} \right), m = m, \\
 &\quad m + 1, \dots, m + W_{sh} - 1 \quad (81)
 \end{aligned}$$

where W_{sh} is the length of sliding window.

- 2) The maximum values of sharpness value are searched nearby the time window selected via IPP.
- 3) Obtaining the positions of the maximum values, the optimal time window can be determined as follows:

$$m_{\text{opt}} = \arg \max_{m \in \mathbf{M}_n} s_h(m) \quad (82)$$

$$T_w^{\text{opt}} = [m_{\text{opt}}^b, m_{\text{opt}}^e] \quad (83)$$

$$L_{\text{opt}} = m_{\text{opt}}^e - m_{\text{opt}}^b + 1 \quad (84)$$

where \mathbf{M}_n represents the nearby area around the time window selected via IPP, m_{opt}^b and m_{opt}^e are the optimal start and end imaging moments, T_w^{opt} represents the optimal time window, and L_{opt} is the optimal TWL. Here, the subdata with the optimal time window is called as optimal subdata.

The high-quality ISAR image with the ship's side or top view can be attained via the proposed OTWD method. Specially, under the low sea condition, the ship ISAR image can obtain the high azimuth resolution.

Remark 4: The IPP is considered to be almost unchanged in the optimal time window. First, the ISAR image with the

optimal time window should be a top or side view of ship target and ensure the optimal image quality and azimuth resolution. If the IPP changes sharply, the ISAR image will give the hybrid view of ship target, which influences the image quality as well. Hence, the IPP is considered to be almost unchanged during the optimal time window. Second, the optimal time window is obtained with the extended subdata, which is combined with three parts of the subdata. Fig. 8 gives a part of curves about the rotation parameter estimation. The time window determined via IPP selection is shown as the green shadow area in Fig. 8. However, the blue ellipse area owns the similar IPP feature. Hence, the IPP will not change obviously in the optimal time window. Given the above, the IPP is considered to be almost unchanged during the imaging interval.

For some special cases, the IPP may change rapidly, such as the high sea condition or high maneuvering ship target. Under these circumstances, we can reduce the size of extended subdata to restrain the variation of IPP.

IV. EXPERIMENTAL RESULT

In this section, we show some results of simulated and real measured data for better illustrating the processing procedures of the proposed OTWD approach. Meanwhile, the results can verify the effectiveness of the OTWD approach. The experiments are consisted of four groups: simulated data under the low sea condition, simulated data under the high sea condition, simulated data with general rotation parameters and shore-based ISAR real measured data.

First, the azimuth size of subapertures need to be determined. The selection standards for the azimuth size of the subaperture can be considered from the aspects of image quality, image proportion, computing time, and parameters estimation. Standards for the azimuth size of subapertures are elaborated as follows.

A. From the Point of Image Quality

With the smaller azimuth size of subapertures, the Doppler frequency is almost steady. Hence, the ISAR image generated by the subdata will be well-focused, which is beneficial to the estimation of rotation parameters. If the azimuth size of subapertures is too large, the Doppler frequency may vary with the observation time, which leads to the azimuth defocus of radar image. Therefore, the azimuth size should not be too large. In this article, the azimuth size of subapertures is 256, and the corresponding accumulating time is about 0.5 s. This is very short compared with the whole rotation period for the ship target, and the Doppler frequency will not be changed obviously during this interval.

B. From the Point of Image Proportion

To ensure the appropriate image proportion, the azimuth resolution need to be closed to range resolution, which can be expressed as $c/(2B_r) \approx \lambda/(2\omega_e N_{as}/PRF)$, where B_r is the bandwidth of echo signal. Hence, the azimuth size can be calculated as $N_{as} \approx \lambda B_r PRF / (c\omega_e)$. After calculation, the azimuth sizes under the low and high sea condition are 646 and

TABLE II
PARAMETERS OF THE RADAR AND IMAGING SCENE

Parameters	Values
Pulse width	10 μ s
Sample frequency	400MHz
Bandwidth	200MHz
Carrier frequency	9.92GHz
PRF	500Hz
Imaging interval	12.2s

161, respectively. Hence, we select 256 pulses as the representative subapertures size under the consideration of fast Fourier transform with convenience.

C. From the Point of Computing Time

With the smaller azimuth size, the computing time of rotational parameter estimation will be reduced. With too large azimuth size, the computing time will be increased, which is disadvantageous for the subsequent procedure.

D. From the Point of Parameter Estimation

Moreover, with the smaller azimuth size, the estimation curves of rotation parameters can be better described. Note that the azimuth size should not be too small, because the low azimuth resolution will decrease the estimated precision of rotation parameters. With the larger azimuth size, the azimuth resolution will be improved. However, some details of estimation curves may be lost, such as the time interval with top or side view of ship target.

Taking the image quality, image proportion, computing time, and parameter estimation into account, we select the 256 pulses as the azimuth size of sub-aperture in this article.

Second, the indexes which metric the image quality need to be introduced. In this article, the following indexes are used.

- 1) *Image entropy*: It can measure the focusing performance of radar images.
- 2) *Pulse number or TWL*: It can metric the azimuth resolution.
- 3) *Azimuth envelope*: It can reflect the effect of azimuth focusing.

Furthermore, the method in [12] is applied for comparison. The radar image generated via the method in [12] can represent the top view or side view of ship target, while the optimal image quality cannot be obtained. Here, the imaging results of subdata are obtained via the method in [12], and the imaging results of optimal subdata are generated via the proposed OTWD approach. The indexes of these radar images are calculated to compare the performance of the method in [12] and the proposed method.

E. Simulated Data Under the Low Sea Condition

This experiment is designed to verify that the proposed OTWD approach can generate the ISAR image with the high quality, high resolution and the ship's top or side view. The radar parameters are listed in Table II. Meanwhile, the ship

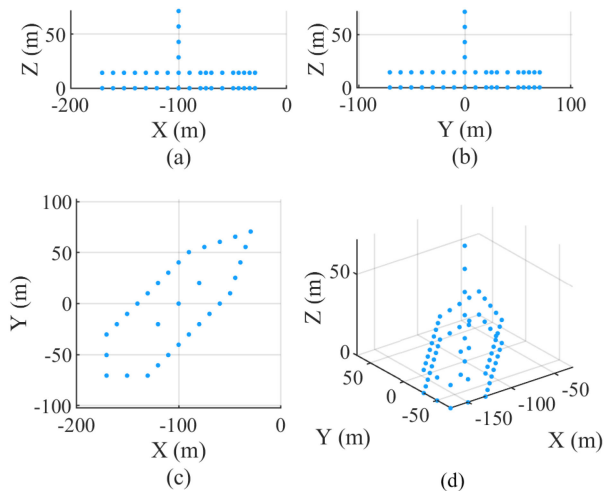


Fig. 11. Ship scatterer model. (a) Front view. (b) Side view. (c) Top view. (d) 3-D view.

TABLE III
ROTATION PARAMETERS OF THE SHIP TARGET

Direction	Amplitude (°)	Average period (s)
Roll	3.48	12.2
Pitch	0.00	12.2
Yaw	3.48	12.2

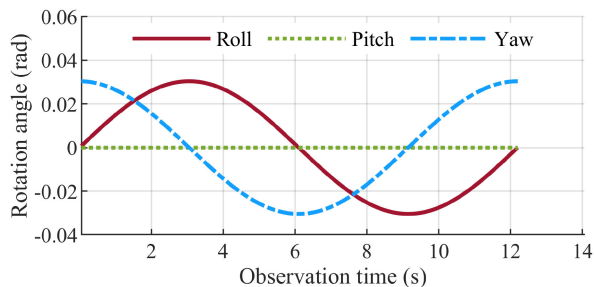


Fig. 12. Rotation angle in different directions.

scatterer model is shown in Fig. 11, where (a)–(d) are the front, side, top, and 3-D view of ship, respectively. As mentioned, the horizontal rotation is related with the roll and pitch rotation, while the vertical rotation is related with yaw rotation. Here, we only use the roll rotation to simulate the horizontal rotation for simplification. The model of rotation angle is same with (55) and the rotation parameters are listed in Table III and $\phi_y = \pi/2$. Fig. 12 gives the rotation angle curve in different directions, where the red solid line, green dotted line, and blue dot dash line represent the rotation angle in the roll, pitch, and yaw, respectively.

Based on the method in [17] and [30], the estimation curves of rotation parameter can be obtained in Fig. 13, where (a) and (b) are the curves of the slope for ship centerline and the azimuth numbers for the Doppler spread, respectively. In Fig. 13, the red marker “x” represents the estimated value, the blue curve is the fitting result with the smooth spline, the yellow dotted line is the zero line, and the red and green shadow area are the time

TABLE IV
TIME WINDOW DETERMINED VIA IPP SELECTION

Number	Top view	Side view
1	[2.8160s, 3.3280s]	[5.8880s, 6.4000s]
2	[8.7040s, 9.2160s]	None

windows selected via the IPP. Obviously, the curves present the tendency of sinusoidal variation. With the principles in Table I, we can obtain the “rough” time windows as listed in Table IV. The time windows of [2.8160 s, 3.3280 s] and [8.7040 s, 9.2160 s] can generate the ISAR image with the ship’s top view. The ISAR image with ship’s side view can be produced with the time window of [5.8880 s, 6.4000 s].

The optimal time window can be acquired via the proposed OTWD method. In this part, we choose the time windows of [8.7040 s, 9.2160 s] and [5.8880 s, 6.4000 s] for optimization.

Remark 5: The rotation parameters of ship target in Table III will not affect the performance about the verification of the proposed OTWD. This group of rotation parameter is designed to distinguish obviously the interval of dominant rotation direction. Since the horizontal rotation is consisted of the roll and pitch rotation, we choose the roll rotation for simulation. Fig. 14 gives the angular velocity in different directions. After calculation, the difference between the absolute horizontal angular velocity and the absolute vertical angular velocity can be obtained as shown in Fig. 15. Apparently, the vertical rotation is dominant absolutely at the moments of 3.0500 and 9.1500 s, while the horizontal rotation is dominant entirely at the moment of 6.1000 s. These dominant moments are conformed to the results in Fig. 13 and Table IV.

1) *Case 1: Optimal Time Window of Top View:* The data in the time window [8.7040 s, 9.2160 s] is corresponding to the 35th subdata, which has 256 pulses. Fig. 16 shows the ISAR image generated by the 35th subdata, which shows the top view of ship target. However, the time window is “rough” and can be optimized for the improvement of image quality and azimuth resolution.

Combining the 33th, 35th, and 37th subdata, we can obtain the extended subdata with 768 pulses. The ISAR imaging results are shown in Fig. 17, where (a), (b), and (c) are the ISAR image, signal energy in each range bin, and TFD result of the 2161th range bin, respectively. In Fig. 17, the ISAR image for the extended subdata shows the ship’s top view as well. Hence, the IPP does not change severely in the time window of extended subdata. Then, the 2161th range bin with a single scatterer is selected. With the TFD result, the Doppler frequency is almost invariable with the observation time as seen in Fig. 17(c).

Based on (77), we can calculate the Doppler frequency estimation value. Fig. 18 gives the estimation curve of Doppler frequency, where the red dots are the estimated values of Doppler frequency and the blue solid line is the fitting result with polynomial. Obviously, the TWL of smooth curve is longer than 0.512 s in Fig. 18.

With the proposed sharpness analysis method, the optimal time window can be generated. Fig. 19 shows the sharpness curve of Doppler frequency. In Fig. 19, the blue solid line is

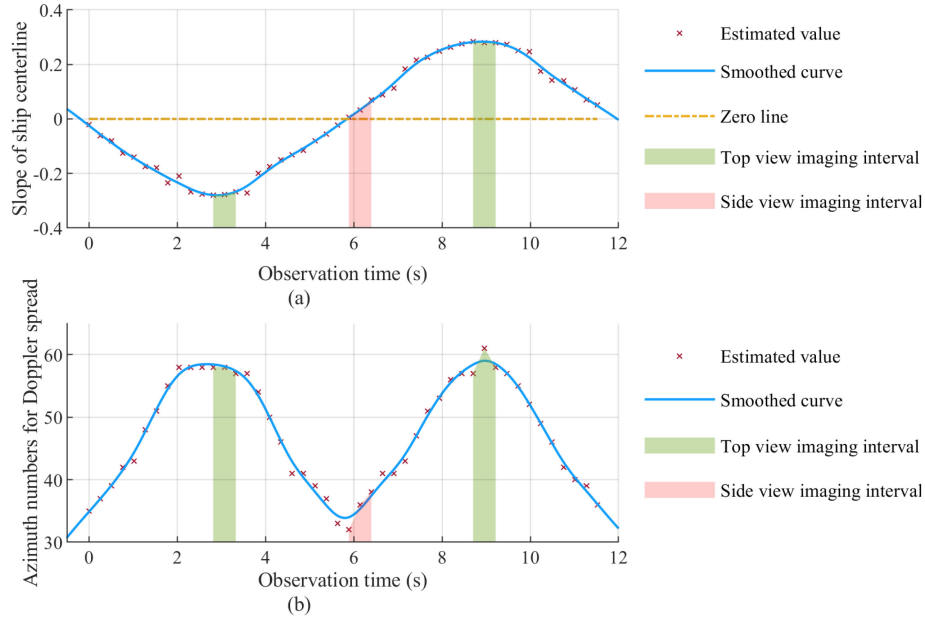


Fig. 13. Curves of rotation parameter estimation. (a) Slope curve of ship centerline. (b) Curve of azimuth numbers for the Doppler spread.

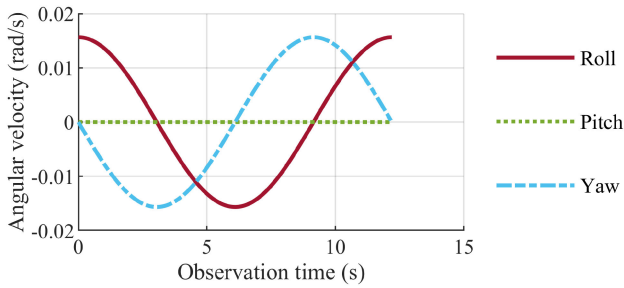


Fig. 14. Angular velocity in different directions.

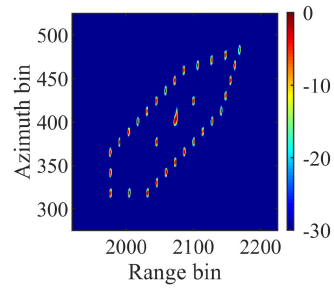


Fig. 16. ISAR image generated by the 35th data.

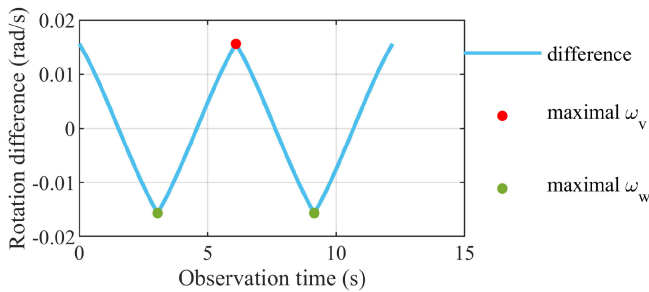


Fig. 15. Absolute difference of angular velocity between the horizontal rotation and vertical rotation.

the sharpness curve, the yellow and purple shadow area are search regions for the optimal start and end imaging moment, the red triangle marker is the maximum value in the search area, and the blue and red dotted line represent the optimal start and end imaging moment. Searching the maximal values around the 8.7040 and 9.2160 s, we obtain the optimal time window of [8.7960 s, 9.6380 s].

Fig. 20 shows the ISAR image generated via the optimal subdata. In this article, we apply the entropy to evaluate the image quality. The definition of image entropy is shown as follows:

$$E(I) = - \sum_m \sum_n \frac{|I(m, n)|^2}{S(I)} \ln \frac{|I(m, n)|^2}{S(I)}. \quad (85)$$

The function $S(I)$ is given in the following:

$$S(I) = \sum_m \sum_n |I(m, n)|^2 \quad (86)$$

where $I(m, n)$ is the ISAR image.

Table V gives the time window, TWL, pulse number, and entropy for ISAR images produced by the subdata, extended subdata, and optimal subdata. For equity, the ISAR images are adjusted by zero-padding as the same azimuth size: 768 pulses. Compared with the time windows in Table V, the optimal end imaging moment does not exist in the time window of subdata, which can illustrate that the combination of extended subdata is effective. Meanwhile, both TWL and pulse number of the

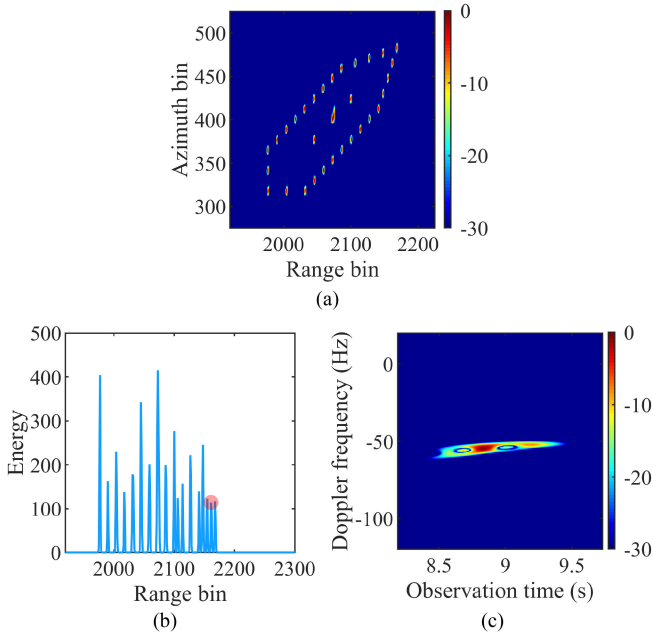


Fig. 17. ISAR imaging results for the extended data. (a) ISAR image. (b) Signal energy in each range bin. (c) TFD result of the range bin with a single scatterer.

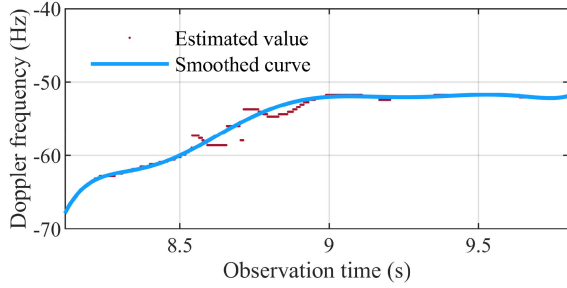


Fig. 18. Doppler frequency estimation curve.

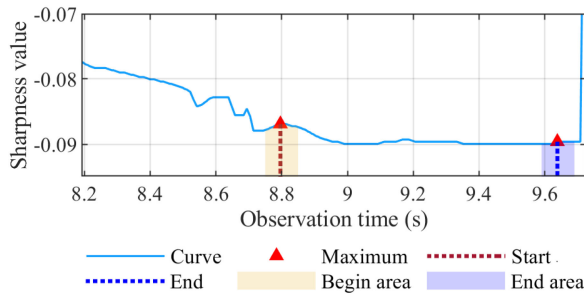


Fig. 19. Sharpness curve of the Doppler frequency estimation value.

TABLE V
TIME WINDOW, TWL, PULSE NUMBER, AND ENTROPY OF DIFFERENT SHIP ISAR IMAGES

	Subdata	Extended subdata	Optimal subdata
Time window	[8.7040s,9.2160s]	[8.1920s,9.728s]	[8.7960s,9.6380s]
TWL	0.512s	1.5360s	0.8420s
Pulse number	256	768	422
Entropy	7.1227	7.4473	6.9078

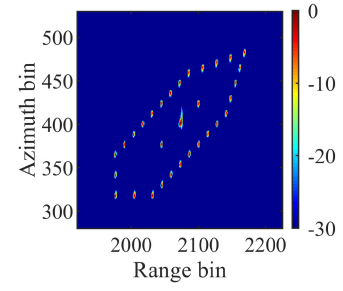


Fig. 20. High quality and high-resolution ISAR image with the top view of ship target.

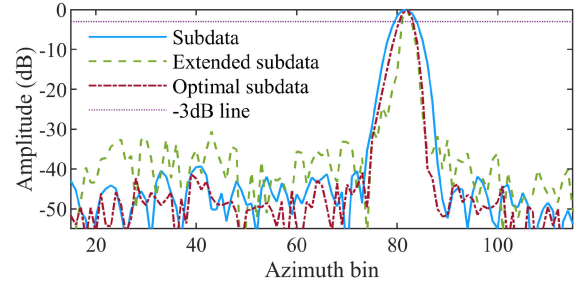


Fig. 21. Comparison of the azimuth resolution.

optimal subdata are larger than that of the subdata. Hence, the proposed OTWD approach can improve the azimuth resolution under the low sea condition. Furthermore, the image entropy for the optimal subdata is the smallest, which can verify that the proposed OTWD method can improve image quality.

Fig. 21 shows the azimuth envelopes for the subdata, extended subdata, and optimal subdata. In Fig. 21, the blue solid line, green dotted line, and red dot dash line represent the envelopes for the subdata, extended subdata, and optimal subdata, respectively. Moreover, the purple dotted line is the -3 dB line. As seen in Fig. 21, the main lobe width for the optimal subdata is between the subdata and extended subdata. Hence, the proposed OTWD method can improve the azimuth resolution and ensure the high image quality simultaneously.

For further verification, we process nonoptimal subdata and compute the image entropy. The nonoptimal subdata owns the same TWL with the optimal subdata. Fig. 19 gives the optimal time window selected via the proposed OTWD approach. The optimal time window is [8.7960 s, 9.6380 s] and TWL is 0.8420 s. We choose a nonoptimal time window of [8.1920 s, 9.0340 s], in which the sharpness value is large and the Doppler frequency is comparatively unstable. The ISAR image for the nonoptimal subdata can be seen in Fig. 22. Compared with the ISAR image in Fig. 20, the ISAR image in Fig. 22 has obvious azimuth defocus. The image entropies of Figs. 20 and 22 are 6.9078 and 7.7607, respectively. Hence, the ISAR image with the nonoptimal time window has poor quality, which can illustrate the effectiveness of the proposed OTWD approach.

2) *Case 2: Optimal Time Window of Side View:* According to Fig. 13, the time window selected by IPP is [5.8880 s, 6.4000 s], which corresponds to the 24th subdata. The ISAR image



Fig. 22. ISAR image with the non-optimal time window.

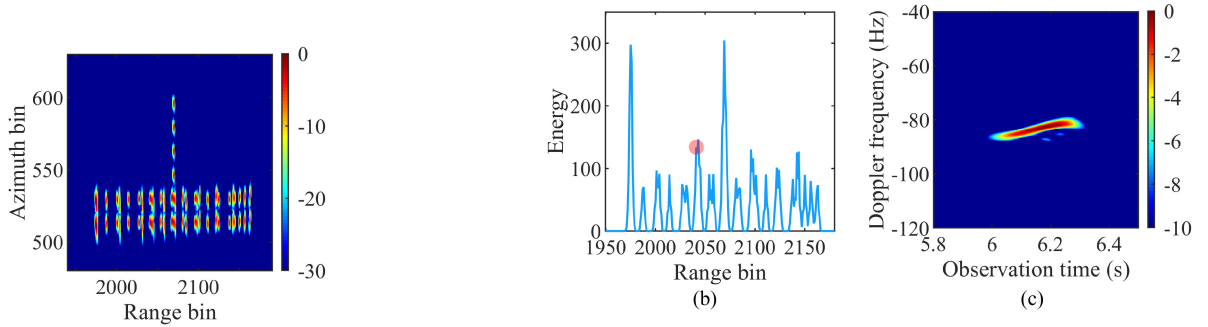


Fig. 23. ISAR image generated by the 24th subdata.

Fig. 24. ISAR imaging results for the extended subdata. (a) ISAR image. (b) Signal energy in each range bin. (c) TFD result of one range bin with a single scatterer.

for the 24th subdata shows the ship’s side view in Fig. 23, while the azimuth resolution is comparatively low. Afterward, the OTWD approach can be applied to improve the image quality and azimuth resolution.

The 22nd, 24th, and 26th subdata are combined as the extended subdata. The ISAR imaging results for the extended data are shown in Fig. 24, where (a), (b), and (c) are the ISAR image, the signal energy in each range bin, and TFD result of the 2041th range bin, respectively. The ISAR image in Fig. 24(a) also reflects the side view of ship target. However, the azimuth defocus is significant, which illustrates that the TWL of 1.5360 s is too long. The optimal time window can be found via the proposed sharpness analysis. The 2041th range bin with one scatterer is selected. Then, the azimuth signal in the 2041th range bin is analyzed via the SPWVD. The result of SPWVD in Fig. 24(c) shows the stationarity of Doppler frequency under the low sea condition.

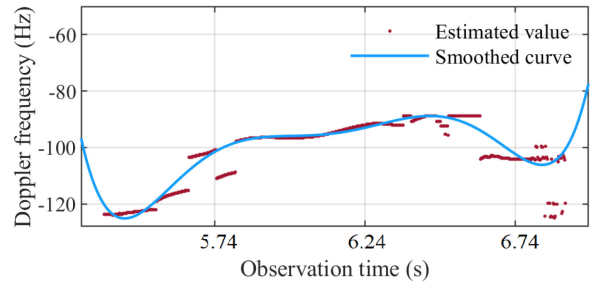


Fig. 25. Doppler frequency estimation curve.

Fig. 25 gives the estimation curve of Doppler frequency, from which we can see that the start and end smooth moment are nearby 5.8880 and 6.4000 s. After the sharpness analysis, we can determine the optimal time window. Fig. 26 shows the result of sharpness analysis. By searching the maximal values around 5.8880 and 6.4000 s, we can find the optimal time window of [5.9380 s, 6.4820 s]. Fig. 27 gives the ISAR image for the optimal subdata, from which we can see that the OTWD approach can attain the ship image with side view. Moreover, the azimuth resolution is higher than the image in Fig. 23 and the image quality is superior than the image in Fig. 24(a).

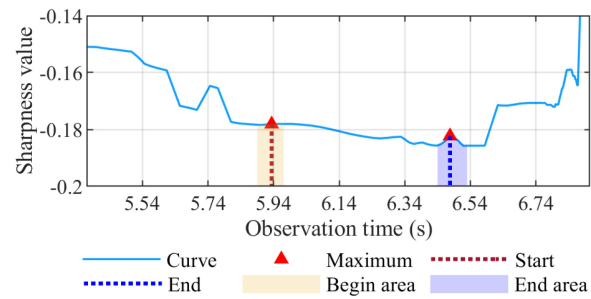


Fig. 26. Sharpness curve of the Doppler frequency estimation value.

Table VI lists the time window, TWL, pulse number, and image entropy for different ship ISAR images. Comparing the time windows, the optimal end imaging moment is not in the time window of subdata. It can illustrate that combining the extended

subdata is necessary and effective. Moreover, the TWL and pulse number of the optimal subdata are larger than that of the subdata. Hence, the proposed OTWD approach can improve the azimuth resolution. Furthermore, the ISAR image for the optimal subdata has the smallest image entropy, which can verify the OTWD approach can enhance the image quality.

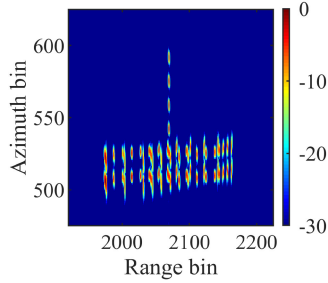


Fig. 27. High quality and high-resolution ISAR image with the side view of ship target.

TABLE VI
TIME WINDOW, TWL, PULSE NUMBER, AND ENTROPY FOR DIFFERENT SHIP ISAR IMAGES

	Subdata	Extended subdata	Optimal subdata
Time window	[5.8880s,6.4000s]	[5.3760s,6.9120s]	[5.9380s,6.4820s]
TWL	0.512s	1.5360s	0.5440s
Pulse number	256	768	273
Entropy	8.1373	8.7814	8.1290

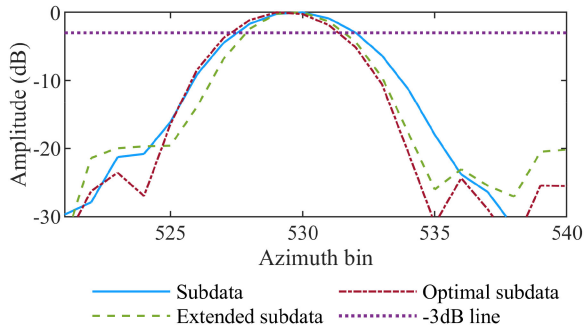


Fig. 28. Comparison of the azimuth resolution.

Fig. 28 gives the azimuth envelopes for the subdata, extended subdata and optimal subdata. The main lobe width for the optimal subdata is between the subdata and extended subdata. Hence, the proposed OTWD method can obtain the optimal azimuth resolution.

F. Simulated Data Under High Sea Condition

Under the high sea condition, the rotation motion is enhanced, which leads to the time-varying Doppler frequency. Hence, the optimal TWL may be shorter than 0.512 s. The proposed OTWD method can produce the well-focused ISAR image with the ship's top or side view, while the azimuth resolution cannot be superior to the ISAR image for the subdata.

We set the rotation amplitude is four times larger than that in Section IV-A to simulate the high sea condition. The detail rotation parameters are listed in Table VII. Fig. 29 depicts the curve of rotation angle.

Fig. 30 gives the curves of rotation parameter estimation. Fig. 30(a) is the slope curve of the ship centerline, which can reflect the variation of vertical rotation. Fig. 30(b) is the curve of

TABLE VII
ROTATION PARAMETERS OF THE SHIP TARGET

Direction	Amplitude (°)	Average period (s)
Roll	13.92	12.2
Pitch	0.00	12.2
Yaw	13.92	12.2

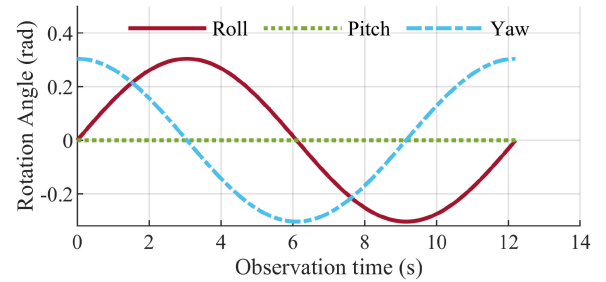


Fig. 29. Rotation angle in different directions.

TABLE VIII
TIME WINDOW DETERMINED VIA IPP SELECTION

Number	Top view	Side view
1	[2.8160s, 3.3280s]	[5.8880s,6.4000s]
2	[8.9600s, 9.4720s]	None

the azimuth numbers for Doppler spread, which can illustrate the change of the effective rotation. After the IPP selection, we can obtain the “rough” time windows, which is shown as the green and red shadow area in Fig. 30. Table VIII lists these “rough” time windows. In this simulation, the echo data with the time windows of [2.8160 s, 3.3280 s] and [8.9600 s, 9.4720 s] can generate the ISAR image with the ship's top view. Moreover, the time window of [5.8880 s, 6.4000 s] is appropriate to produce the ISAR image with the ship's side view. Here, we choose the time windows of [2.8160 s, 3.3280 s] and [5.8880 s, 6.4000 s] for optimization via the OTWD approach.

1) *Case 1: Optimal Time Window of Top View:* The subdata with the time window [2.8160 s, 3.3280 s] is corresponding to the 12th subdata. Fig. 31 gives the ISAR image for the 12th subdata. Obviously, the image quality is lower than the image in Fig. 16, which can reflect that the Doppler frequency is time-varying and lead to azimuth defocus under the high sea condition.

By combining the 10th, 12th, and 14th subdata, the extended subdata can be generated. Fig. 32(a) gives the ISAR image for the extended subdata. Fig. 32(b) gives the signal energy in each range bin and we select the 2001th range bin for the calculation of TFD. The TFD result is shown in Fig. 32(c), which can depict that the Doppler frequency is slightly varied with the observation time.

The Doppler frequency is estimated via (77) and the estimated values is fitted by polynomial. Fig. 33 shows the estimation curve of Doppler frequency. The green rectangle shows the smooth part of the Doppler frequency curve, which indicates that the TWL is shorter than 0.512 s. Obviously, the start and end optimal moment are around 2.8160 and 3.3280 s. Then, the sharpness analysis can be implemented.

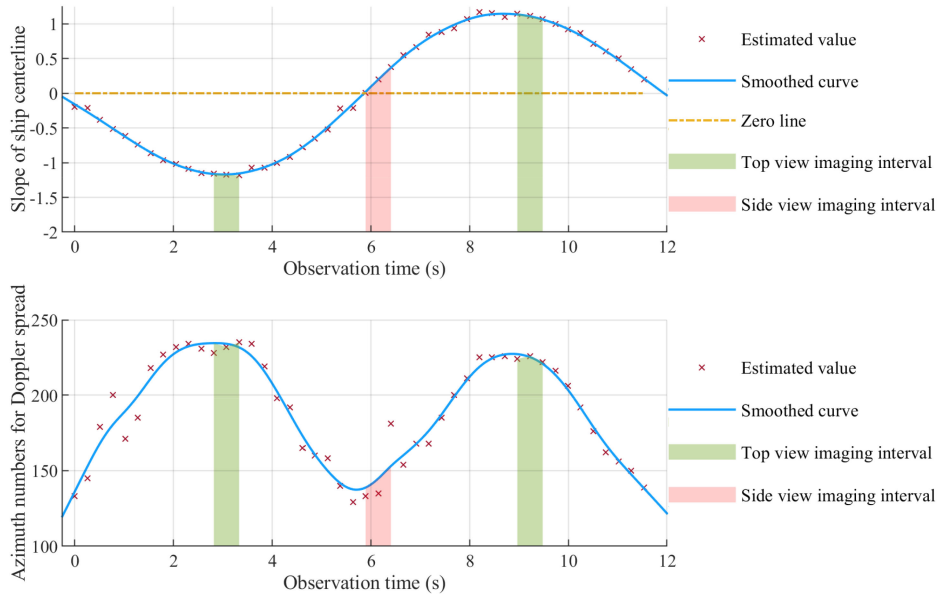


Fig. 30. Curves of the rotation parameter estimation. (a) Slope curve of ship centerline. (b) Curve of the azimuth numbers for the Doppler spread.

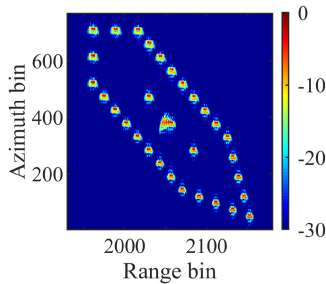


Fig. 31. ISAR image generated by the 12th subdata.

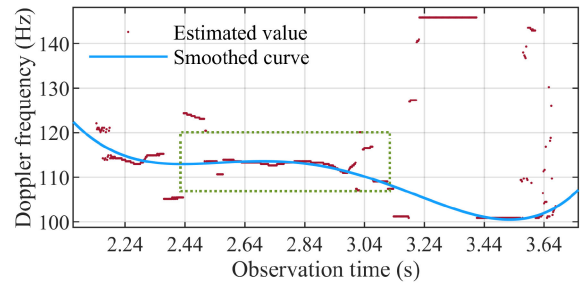
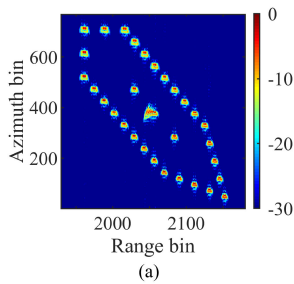
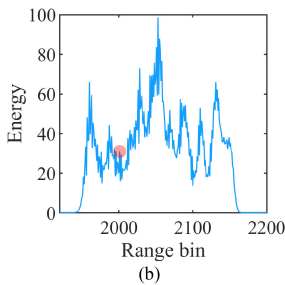


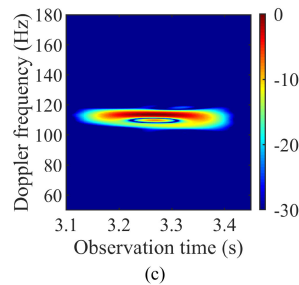
Fig. 33. Doppler frequency estimation curve.



(a)



(b)



(c)

Fig. 32. ISAR imaging results for the extended subdata. (a) ISAR image. (b) Signal energy in each range bin. (c) TFD result of one range bin with a single scatterer.

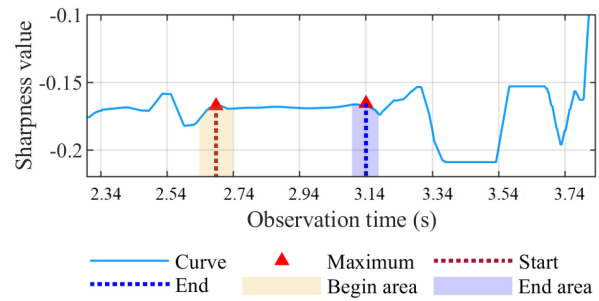


Fig. 34. Sharpness curve of the Doppler frequency estimation value.

Fig. 34 shows the sharpness curve of the Doppler frequency estimated value. Searching the maximal value around 2.8160 and 3.3280 s, we can determine the optimal time window of [2.6920 s, 3.1440 s]. Fig. 35 shows the ISAR image for the optimal subdata, which can reflect that the proposed OTWD approach can determine the IPP of ISAR image.

Table IX gives the time window, TWL, pulse number, and image entropy for the subdata, extended subdata, and optimal

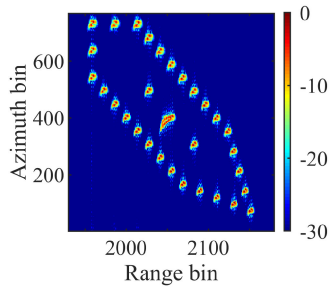


Fig. 35. High quality ISAR image with the top view of ship target.

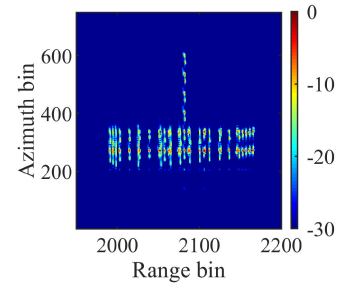


Fig. 37. ISAR image generated by the 24th subdata.

TABLE IX
TIME WINDOW, TWL, PULSE NUMBER, AND ENTROPY OF DIFFERENT SHIP ISAR IMAGES

	Subdata	Extended subdata	Optimal subdata
Time window	[2.8160s,3.3280s]	[2.3040s,3.8400s]	[2.6920s,3.1440s]
TWL	0.512s	1.5360s	0.4520s
Pulse number	256	768	227
Entropy	9.5701	10.1408	9.5310

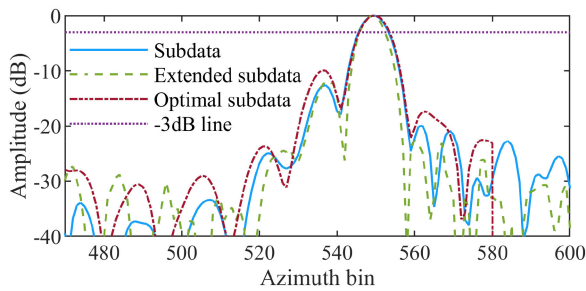


Fig. 36. Comparison of the azimuth resolution.

subdata. The optimal start imaging moment is outside the time window of subdata, which can illustrate that generating the extended subdata is beneficial. Furthermore, the TWL and pulse number for the optimal subdata are smaller than that for the subdata. This phenomenon is caused by the time-varying Doppler frequency. Meanwhile, the improvement of azimuth resolution is restrained under the high sea condition. Moreover, the entropy for the ISAR image of optimal subdata is the smallest, which shows the highest image quality. Hence, the image quality can be improved via the OTWD approach.

Fig. 36 gives the azimuth envelopes for the subdata, extended subdata, and optimal subdata. The main lobe width for the optimal subdata is the widest, but closed to the main lobe width for the subdata. Therefore, the OTWD approach can provide the optimal azimuth resolution under the high sea condition.

2) *Case 2: Optimal Time Window of Side View:* The subdata with the time window of [5.8880 s, 6.4000 s] corresponds to the 24th subdata. Fig. 37 shows the ISAR image of the 24th subdata, which represents the well-focused side view of ship target.

Before the OTWD approach, the 22th, 24th, and 26th subdata are combined as the extended subdata. Fig. 38 shows the imaging results for the extended subdata, where (a), (b), and (c) are the

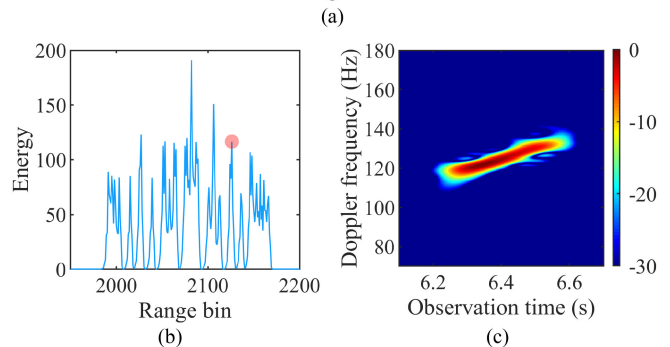
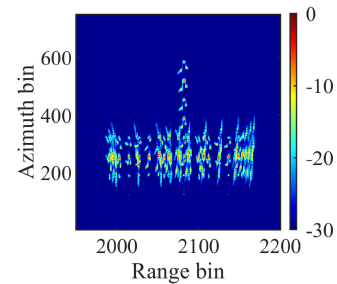


Fig. 38. ISAR imaging results for the extended data. (a) ISAR image. (b) Signal energy in each range bin. (c) TFD of one range bin with a single scatterer.

ISAR image, the signal energy in each range bin, and the TFD result of the 2126th range bin. Obviously, the ISAR image is severely defocused in the azimuth direction, which reflects the sharp variation of Doppler frequency during the observation time of 1.5360 s. In Fig. 38(b), we choose the 2126th range bin with a single scatterer for Doppler frequency analysis. Apparently, the Doppler frequency changes significantly with the slow time in Fig. 38(c), which leads to the azimuth defocus in Fig. 38(a).

Fig. 39 shows the estimation curve of Doppler frequency. The curve in the green rectangle is almost smooth. Meanwhile, the optimal start and end moment can be searched around 5.8880s and 6.4000 s. Then, the sharpness analysis is implemented.

Fig. 40 gives the sharpness curve of Doppler frequency. After calculation, the optimal time window is determined as [5.8600 s, 6.3460 s]. Moreover, the ISAR image with the optimal time window is shown in Fig. 41, whose image quality is obviously higher than Fig. 37. Hence, the proposed OTWD approach can improve the quality of ISAR image.

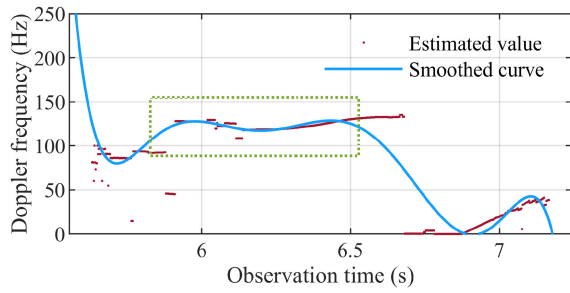


Fig. 39. Doppler frequency estimation curve.

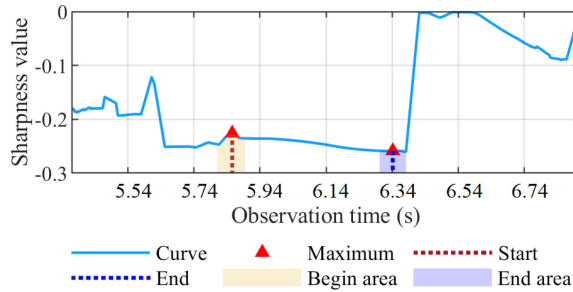


Fig. 40. Sharpness curve of the Doppler frequency estimation value.

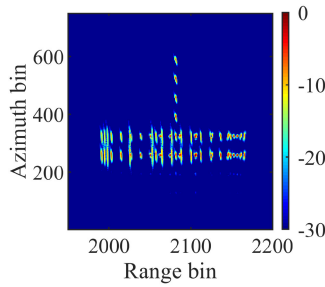


Fig. 41. High-quality ISAR image with the side view of ship target.

TABLE X
TIME WINDOW, TWL, PULSE NUMBER, AND ENTROPY OF DIFFERENT SHIP ISAR IMAGES

	Subdata	Extended subdata	Optimal subdata
Time window	[5.8880s,6.4000s]	[5.6320s,7.1660s]	[5.8600s,6.3460s]
TWL	0.512s	1.5360s	0.4860s
Pulse number	256	768	244
Entropy	9.3493	9.8913	9.1279

The time window, TWL, pulse number, and image entropy for the subdata, extended subdata, and optimal subdata are listed in Table X. The optimal start imaging moment is not in the time window for the subdata. Hence, generating the extended subdata is beneficial for OTWD. The pulse number and TWL for the optimal subdata are the smallest, which cause the lower azimuth resolution. Furthermore, the ISAR image with the optimal time window has the smallest entropy and the highest quality.

The azimuth envelopes for the subdata, extended subdata, and optimal subdata are shown in Fig. 42. The main lobe width

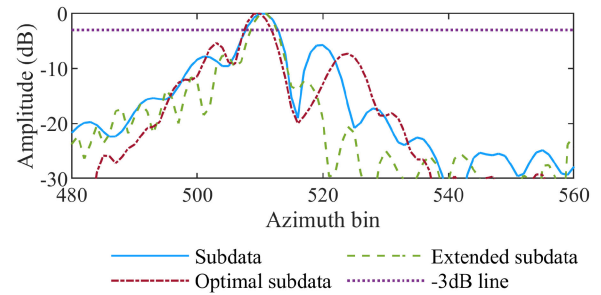


Fig. 42. Comparison of the azimuth resolution.

TABLE XI
ROTATION PARAMETERS OF THE SHIP TARGET

Direction	Amplitude (°)	Average period (s)
Roll	5.00	26.4
Pitch	1.90	11.2
Yaw	7.33	15.6

TABLE XII
TIME WINDOW DETERMINED VIA IPP SELECTION PRINCIPLE

Number	Top view	Side view
1	[0.2560s, 0.7680s]	[3.5840, 4.0960s]
2	[7.9360s, 8.4480s]	[11.5200s, 12.0320s]
3	[14.3360s, 14.8480s]	None

for the subdata and optimal subdata are almost same. Hence, the proposed OTWD method can provide the optimal azimuth resolution.

G. Simulated Data With General Rotation Parameters

Another simulation experiment with the general rotation parameters is set to verify the effectiveness of the proposed approach. This group of general rotation parameters are listed in Table XI. Fig. 43 shows the estimation curves of rotation parameters, where (a) and (b) represent curves of the ship's centerline slope and Doppler spread, respectively. Table XII lists the time windows of subdata that can generated the ISAR image with the ship's top view and side view.

The time window of [7.9360 s, 8.4480 s] is selected to implement the proposed approach. Fig. 44 gives the ISAR image generated via by the 32th subdata, which presents the ship's top view. The ISAR image in Fig. 44 has a slight azimuth defocus.

Then, the extended subdata is generated and Fig. 45(a) gives the ISAR imaging result of the extended subdata. Obviously, the ISAR image in Fig. 45(a) has a more serious azimuth defocus. We choose the 2031th range bin for the TFD calculation as seen in Fig. 45(b). The TFR of the 2031th range bin is shown in Fig. 45(c). Afterward, the Doppler frequency is estimated based on Fig. 45(c). The estimation result can be seen in Fig. 46. After the sharpness analysis, the sharpness curve can be obtained as shown in Fig. 47. With the search of maximum, the optimal time window can be determined as [8.0340 s,8.3620 s]. Fig. 48 is the ISAR image produced with the optimal time window. Compared with Fig. 45(a), Fig. 48 has the higher image quality.

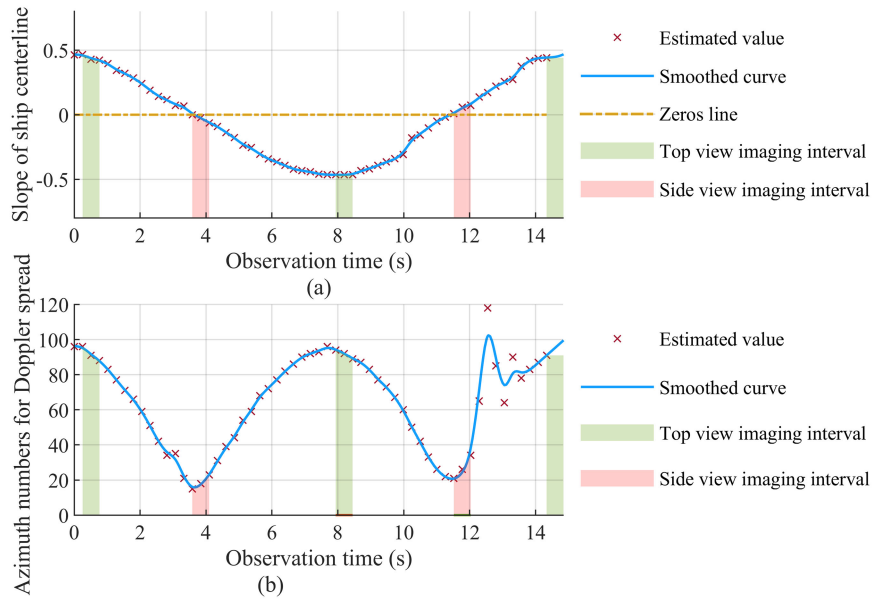


Fig. 43. Curves of the rotation parameter estimation. (a) Slope of ship centerline. (b) Curve of the azimuth numbers for the Doppler spread.



Fig. 44. ISAR image generated by the 32th subdata.

TABLE XIII
TIME WINDOW, TWL, PULSE NUMBER, AND ENTROPY OF DIFFERENT SHIP ISAR IMAGES

	Subdata	Extended subdata	Optimal subdata
Time window	[7.9360s,8.4480s]	[7.424s,8.9600s]	[8.0340s,8.3620s]
TWL	0.512s	1.5360s	0.3280s
Pulse number	256	768	164
Entropy	8.2784	9.2646	8.0968

For further verifying the performance of the proposed approach, the time windows, TWLs, pulse numbers, and image entropies of the subdata, extended subdata, and optimal subdata are listed in Table XIII. After comparison, we can see that the ISAR image generated with the optimal time window has the highest image quality. Meanwhile, TWL of the optimal subdata is the shortest. Hence, the ISAR image with the optimal subdata should have a lower azimuth resolution than the ISAR image with the subdata. Afterwards, we choose the 2031th range bin to compare the azimuth envelopes of the subdata, extended subdata, and optimal subdata as shown in Fig. 49. The main

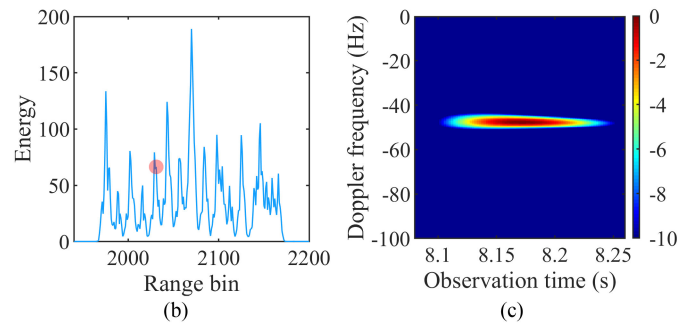


Fig. 45. ISAR imaging results for the extended data. (a) ISAR image. (b) Signal energy in each range bin. (c) TFD of one range bin with a single scatterer.

lobe width of the optimal time window is almost closed to the subdata and extended subdata.

H. Real Measured Data

The shore-based ISAR real measured data is processed for verifying the effectiveness of the proposed OTWD approach. Table XIV lists the parameters of the real measured data, we can see that observation time for the ship target can reach

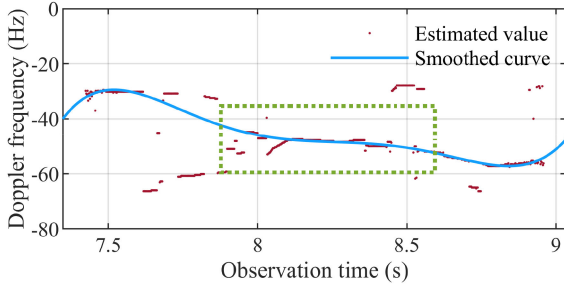


Fig. 46. Doppler frequency estimation curve.

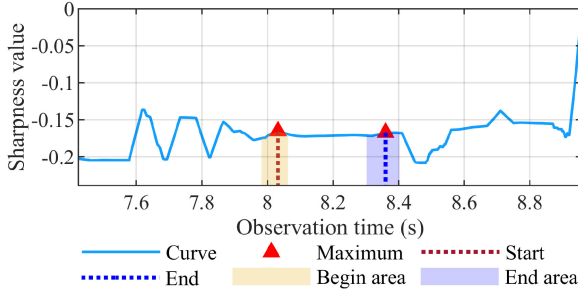


Fig. 47. Sharpness curve of the Doppler frequency estimation value.

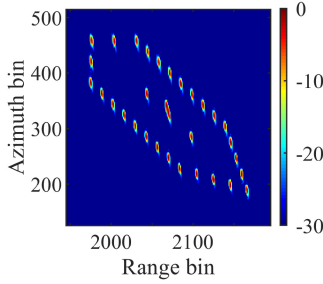


Fig. 48. High-quality ISAR image with the top view of ship target.

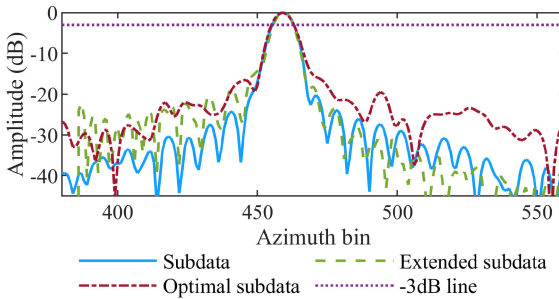


Fig. 49. Comparison of the azimuth resolution.

TABLE XIV
PARAMETERS OF THE REAL MEASURED DATA

Parameters	Values
Bandwidth	200MHz
Carrier frequency	X band
PRF	500Hz
Number of range bin	962
Entire imaging interval	55.296s

TABLE XV
TIME WINDOW DETERMINED VIA IPP SELECTION PRINCIPLE

Number	Top view	Side view
1	[8.1920s, 8.7040s]	[0.2560s, 0.7680s]
2	[21.248s, 21.760s]	[23.808s, 24.320s]
3	[38.144s, 38.656s]	[26.624s, 27.136s]
4	[49.408s, 49.920s]	[34.560s, 35.072s]
5	None	[43.264s, 43.776s]

55.296 s. Obviously, processing the entire data will induce the severe defocus of the ISAR image and appear the ship's hybrid view simultaneously. Hence, the optimal time window should be determined for achieving the well-focused and high-resolution ISAR image with the ship's top or side view.

Fig. 50 shows the estimation curves of the rotation parameters, where (a) is the slope curve of the ship centerline and (b) is the curve of azimuth numbers for the Doppler spread. The curves in Fig. 50(a) and (b) can reflect the change of vertical and effective rotation. The green and red shadow area in Fig. 50 shows the "rough" time windows determined by IPP. These "rough" time windows are listed in Table XV.

As seen in Fig. 50, some fluctuations occur on the estimated values owing to the complicated electromagnetism environment. Taking the time interval of [46.60 s, 51.46 s] as example, the estimated values increase gradually in the time window of [46.60 s, 50.43 s], and decrease in the time window of [50.43 s, 51.46 s]. Hence, despite being affected by the fluctuation, the trends of centerline slope and Doppler spread are synchronous in fact. Moreover, the centerline slope and Doppler spread reach the maximal value and minimal value in the time window of [49.408 s, 49.920 s], respectively, which can reflect that the vertical rotation is dominant.

In this experiment, we choose the time windows [49.408 s, 49.920 s] and [34.560 s, 35.072 s] for optimization via the proposed OTWD approach, respectively.

1) *Case 1: Optimal Time Window of Top View:* The subdata with the time window [49.408 s, 49.920 s] corresponds to the 194th subdata. Fig. 51 gives the ISAR image for the 194th subdata, which shows the ship's top view. Obviously, the azimuth resolution for the ship image is not ideal. Hence, we can implement the proposed OTWD approach for improvement of the image quality and azimuth resolution.

Then, the 192th, 194th, and 196th subdata are combined as the extended subdata. The imaging results for the extended subdata are shown in Fig. 52, where (a), (b), and (c) represent the ISAR image with the ship's top view, signal energy in each range bin, and TFD result of the 203th range bin, respectively. Obviously, the azimuth resolution for the ISAR image in Fig. 52(a) is higher than that in Fig. 51. Then, we select the 203th range bin with a single scatterer for the calculation of TFD. The TFD result depicts that the Doppler frequency is almost unchanged with the slow time.

After frequency estimation with (77), we can obtain the curve of Doppler frequency in Fig. 53. The start and end smooth moment for the curve are around 49.408 and 49.920 s. Meanwhile, the smooth duration is longer than 0.512 s. The smooth of the

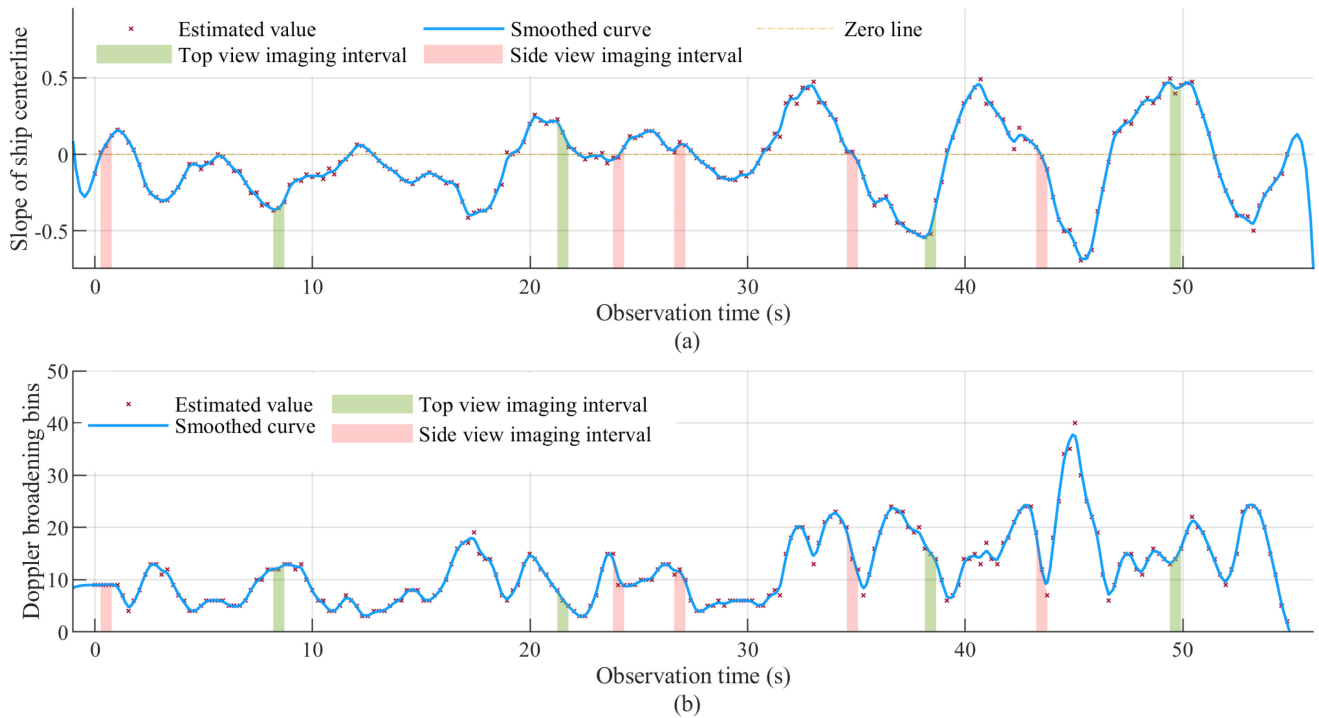


Fig. 50. Curves of the rotation parameter estimation. (a) Slope curve of ship centerline. (b) Curve of the azimuth numbers for the Doppler spread.



Fig. 51. ISAR image generated by the 194th subdata.

Doppler frequency curve is measured via the sharpness analysis. Fig. 54 shows the sharpness curve of the Doppler frequency. After searching the maximal values around 49.408 and 49.920 s, the optimal time window can be determined as [49.2940 s, 50.1060 s].

Fig. 55 gives the ISAR image with the optimal time window. The top view of ship in Fig. 55 can illustrated that the proposed OTWD approach will not change the IPP of ISAR image. Meanwhile, the azimuth resolution for the ship image in Fig. 55 is improved compared with the image in Fig. 51. Moreover, the image quality is superior than the image in Fig. 52(a).

Table XVI lists the time window, TWL, pulse number, and image entropy of the subdata, extended subdata, and optimal subdata. The optimal start and end imaging moment do not exist in the time window of the subdata. Hence, the procedure of generating extended subdata is necessary and effective.

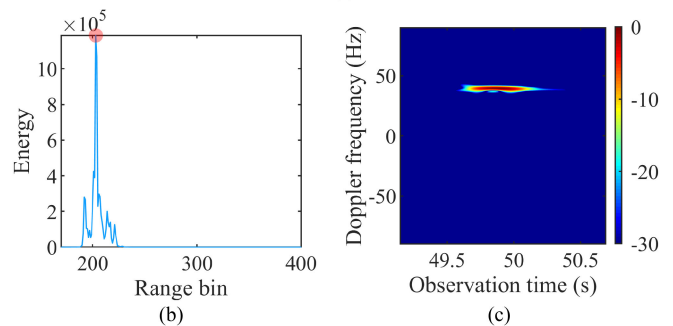


Fig. 52. ISAR imaging results for the extended subdata. (a) ISAR image. (b) Signal energy in each range bin. (c) TFD of one range bin with a single scatterer.

Moreover, the TWL and pulse number of the optimal time window is larger than that of the subdata. Hence, the proposed OTWD approach can improve the azimuth resolution. Furthermore, the ISAR image produced via the proposed OTWD approach has the smallest entropy and the highest quality.

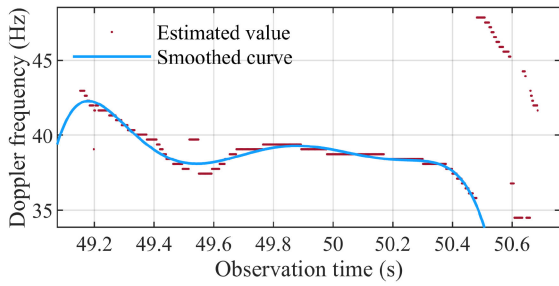


Fig. 53. Doppler frequency estimation curve.

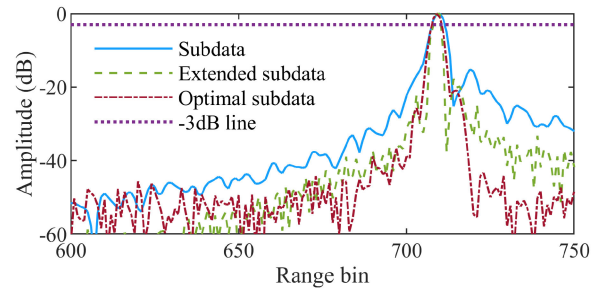


Fig. 56. Comparison of the azimuth resolution.

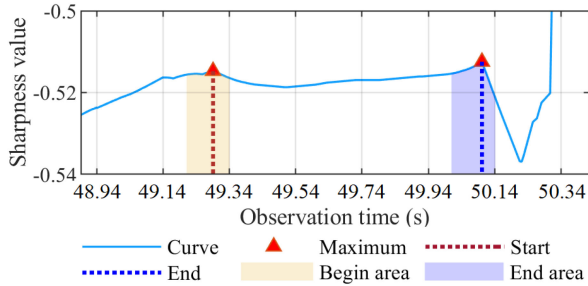


Fig. 54. Sharpness curve of the Doppler frequency estimation value.

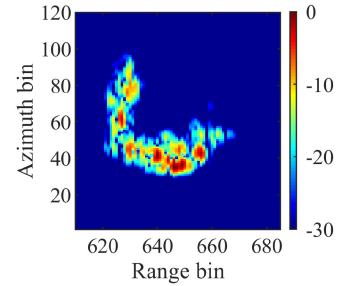


Fig. 57. ISAR image generated by the 136th subdata.

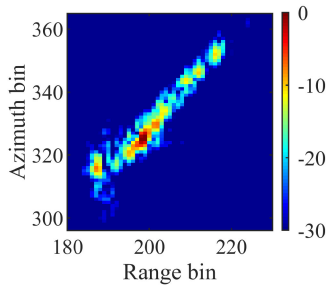


Fig. 55. High-quality and high-resolution ISAR image with the top view of ship target.

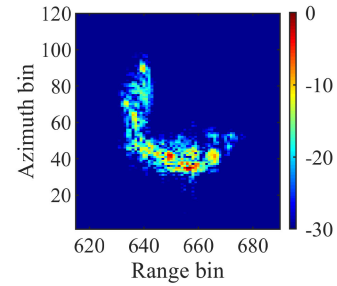


TABLE XVI
TIME WINDOW, TWL, PULSE NUMBER, AND ENTROPY OF DIFFERENT SHIP ISAR IMAGES

	Subdata	Extended subdata	Optimal subdata
Time window	[49.408s,49.920s]	[48.896s,50.430s]	[49.294s,50.106s]
TWL	0.512s	1.5360s	0.812s
Pulse number	256	768	407
Entropy	4.9466	5.1745	4.9391

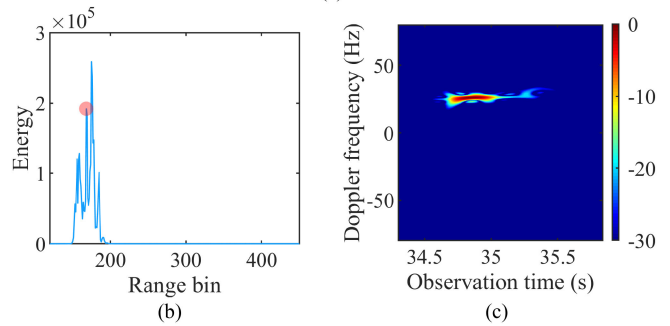


Fig. 58. ISAR imaging results for the extended data. (a) ISAR image. (b) Signal energy in each range bin. (c) TFD of one range bin with a single scatterer.

Fig. 56 gives the azimuth envelopes for the subdata, extended subdata, and optimal subdata. The main lobe width for the optimal subdata is between the subdata and extended subdata. Hence, the proposed OTWD approach can provide the optimal azimuth resolution.

2) *Case 2: Optimal Time Window of Side View:* The subdata with the time window [34.560 s, 35.072 s] is corresponding to the 136th subdata. Fig. 57 gives the ship image of the 136th subdata. The azimuth resolution is comparatively low. Before the OTWD

approach, the 134th, 136th, and 138th subdata are combined as the extended subdata. Fig. 58 shows the imaging results for the extended subdata, where (a) is the ISAR image, (b) is the signal energy in each range bin, and (c) is the TFD result of the 168th range bin. Both Fig. 57 and Fig. 58(a) represent the side view of ship target. Here, we choose the 168th range bin with one scatterer for TFD calculation. The result of TFD in Fig. 58(c) can depict that Doppler frequency is almost unchanged with the observation time.

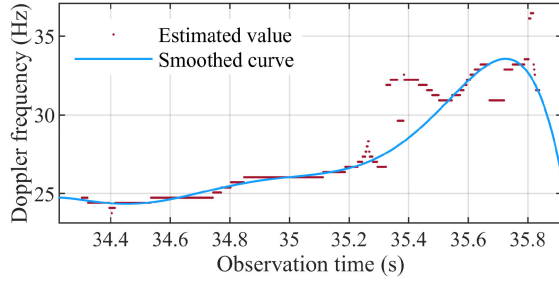


Fig. 59. Doppler frequency estimation curve.

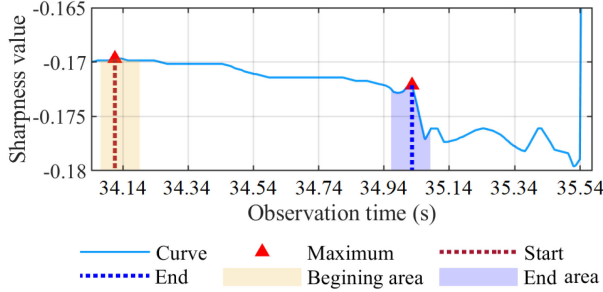


Fig. 60. Sharpness curve of the Doppler frequency estimation value.

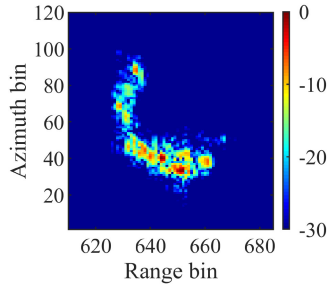


Fig. 61. High-quality and high-resolution ISAR image with the side view of ship target.

TABLE XVII
TIME WINDOW, TWL, PULSE NUMBER, AND ENTROPY OF DIFFERENT SHIP ISAR IMAGES

	Subdata	Extended subdata	Optimal subdata
Time window	[34.560s,35.072s]	[33.608s,35.542s]	[34.120s,35.030s]
TWL	0.512s	1.5360s	0.9100s
Pulse number	256	768	456
Entropy	6.4118	6.3737	6.3155

Then, the Doppler frequency is estimated and Fig. 59 shows the estimation curve of the Doppler frequency. We can observe that the optimal start and end moment are around 34.560 and 35.072 s. Afterward, the sharpness of the Doppler frequency is calculated for OTWD. Fig. 60 shows the sharpness curve. The optimal time window is [34.120 s,35.030 s]. Fig. 61 gives the ship ISAR image with the optimal time window.

Table XVII lists the time window, TWL, pulse number, and image entropy for the subdata, extended subdata, and optimal

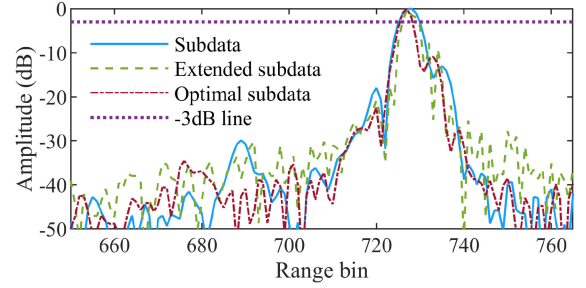


Fig. 62. Comparison of the azimuth resolution.

subdata. Obviously, the optimal start imaging moment is not in the time window of subdata. Hence, the generation of extended subdata should be implemented. Moreover, the TWL and pulse number are larger than 0.512 s and 256. Fig. 62 gives the azimuth envelope for the subdata, extended subdata, and optimal subdata. The main lobe width for the optimal subdata is between the subdata and the extended subdata. Consequently, the proposed OTWD approach can improve the azimuth resolution. Furthermore, the ISAR image with the optimal time window has the smallest entropy, which can illustrate the proposed method can improve the image quality.

I. Different Overlap Lengths of Sliding Window

In this article, the overlap length of sliding window is selected as $N_{as}/2$, which is reasonable for the real measured data. Under the low sea condition, the movement of ship target is smooth, and the variation of IPP is steady. Hence, the short overlap length will be more appropriate, because too long overlap length will increase the computational complexity. Under the high sea condition, the IPP changes rapidly owing to the maneuvering motion of ship target. Correspondingly, too short overlap length may not describe all variation of target motion and the long overlap should be selected. Taking into account the different sea conditions, the overlap length of sliding window is selected as $N_{as}/2$ in this article.

In addition, the experiment results when the overlap length of sliding window is 0 are shown for comparison. The curves of rotation parameter estimation when the overlap length of sliding window is $N_{as}/2$ and 0 are shown in Figs. 50 and 63, respectively. In Fig. 63, the green and red shadow area represent the same time windows of top or side view as that in Fig. 50, respectively, and the yellow and purple shadow area are the reselected time windows of top or side view based on the IPP principle, respectively. Obviously, only two time windows are the same as Fig. 50 and the number of time windows are decreased, which can demonstrate that too short overlap length is inappropriate and unreasonable.

Furthermore, the ISAR imaging results with different time windows are shown to illustrate the disadvantage of short overlap length. With the overlap length of $N_{as}/2$, the time window of top view is selected as [38.1440 s, 38.6560 s]. With the overlap length of 0, the time window of top view is selected as [38.4000 s, 38.9120 s]. The ISAR images with these time windows are shown in Fig. 64(a) and (b). Obviously, compared

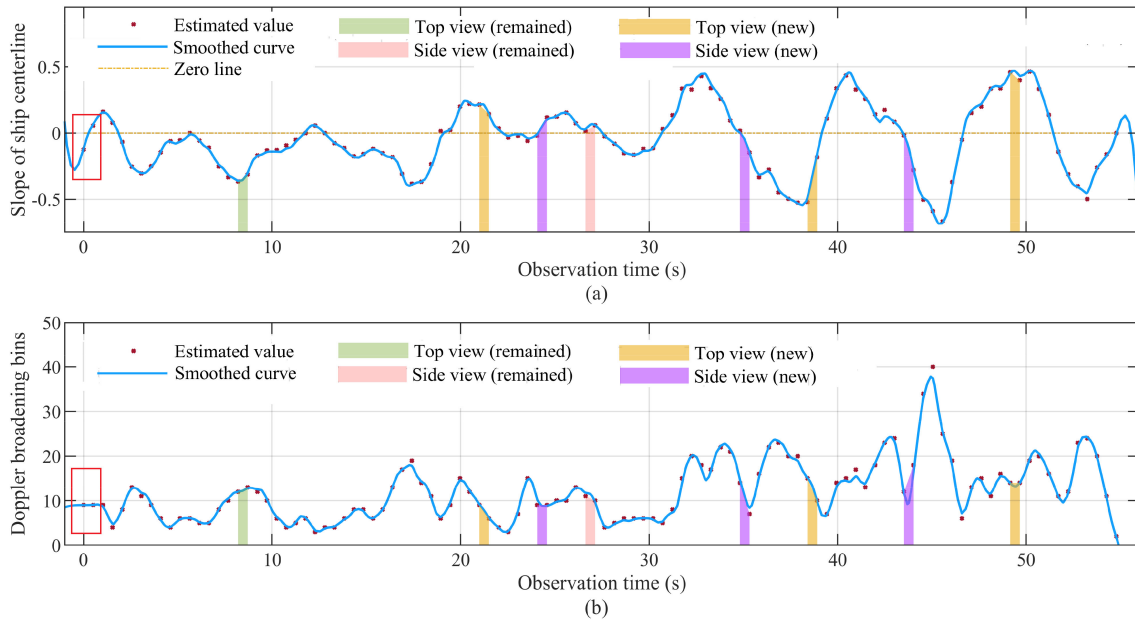


Fig. 63. Curves of the rotation parameter estimation when the overlap length of sliding window is 0. (a) Slope curve of ship centerline. (b) Curve of the azimuth numbers for the Doppler spread.

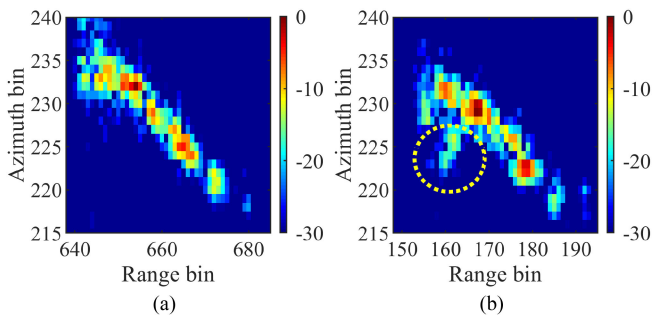


Fig. 64. ISAR image with different overlap lengths of sliding window. (a) Overlap length is $N_{as}/2$, and (b) Overlap length is 0.

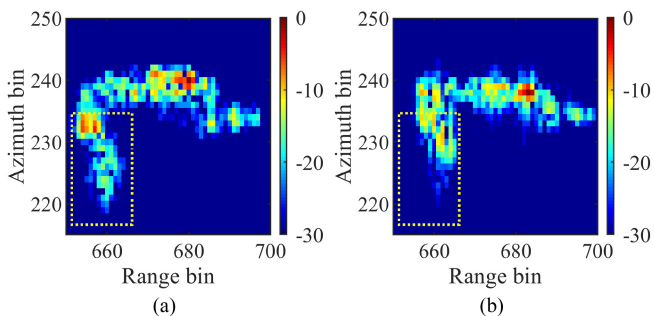


Fig. 65. ISAR image with different overlap lengths of sliding window. (a) Overlap length is $N_{as}/2$, and (b) Overlap length is 0.

with Fig. 64(a), the ISAR image with the overlap length of 0 in Fig. 64(b) is not perfect top view of ship target and represent the hybrid view of ship target as seen in the yellow circle.

With the overlap length of $N_{as}/2$, the time window of side view is selected as [43.2640 s, 43.7760 s]. With the overlap length of 0, the time window of side view is selected as [43.5200 s, 44.0320 s]. The ISAR images with these time windows are

shown in Fig. 65(a) and (b). Similarly, compared with Fig. 65(a), the ISAR image with the overlap length of 0 in Fig. 65(b) is not the perfect side view of ship target, which can be reflected by the shorter ship mast in the yellow rectangles.

Given the above, the overlap length of sliding window is reasonable to select as $N_{as}/2$ for adapting various sea conditions.

V. CONCLUSION

In this article, a novel OTWD approach is proposed for generating the ship ISAR image with single view, high quality and high resolution. The proposed OTWD approach includes the IPP selection, TFD calculation, Doppler frequency estimation, and sharpness analysis. First, the ISAR image can depict the ship's top or side view via the IPP selection method and the "rough" time window can be obtained. Then, the extended subdata is combined and the range bin with a single scatterer is selected. Finally, the optimal time window can be generated via the TFD calculation for the azimuth signal and the sharpness analysis for the Doppler frequency. Furthermore, for the range bin with multiple scatterers, a novel TFD extraction approach based on the clustering analysis is proposed. Results of simulated and real measured data show that the OTWD method can generate an ISAR image for the ship's top or side view with high quality and high resolution.

REFERENCES

- [1] J. B. Zheng, T. Su, G. S. Liao, H. Liu, Z. Liu, and Q. H. Liu, "ISAR imaging for fluctuating ships based on a fast bilinear parameter estimation algorithm," *IEEE J. Sel. Topics Appl. Earth Observ. Remote Sens.*, vol. 8, no. 8, pp. 3954–3966, Aug. 2015.
- [2] J. B. Zheng, H. W. Liu, G. S. Liao, T. Su, Z. Liu, and Q. H. Liu, "ISAR imaging of nonuniformly rotating targets based on generalized decoupling technique," *IEEE J. Sel. Topics Appl. Earth Observ. Remote Sens.*, vol. 9, no. 1, pp. 520–532, Jan. 2016.

- [3] J. B. Zheng, H. W. Liu, G. S. Liao, T. Su, Z. Liu, and Q. H. Liu, "ISAR imaging of targets with complex motions based on a noise-resistant parameter estimation algorithm without nonuniform axis," *IEEE Sens. J.*, vol. 16, no. 8, pp. 2509–2518, Apr. 2016.
- [4] P. H. Huang, X. G. Xia, M. Y. Zhan, X. Liu, G. Liao, and X. Jiang, "ISAR imaging of a maneuvering target based on parameter estimation of multicomponent cubic phase signals," *IEEE Trans. Geosci. Remote Sens.*, vol. 60, Jan. 2022, Art. no. 5103918.
- [5] P. H. Huang *et al.*, "High-resolution ISAR imaging for maneuvering targets based on iterative adaptive processing," *IEEE Trans. Comput. Imag.*, vol. 7, pp. 1093–1108, Oct. 2021.
- [6] P. H. Huang, G. S. Liao, X. G. Xia, Z. Yang, and J. Ma, "A novel algorithm for ISAR imaging based on parameter estimation of cubic phase signal," in *Proc. CIE Int. Conf. Radar*, 2016, pp. 1–5.
- [7] J. B. Zheng, T. Su, L. Zhang, W. Zhu, and Q. H. Liu, "ISAR imaging of targets with complex motion based on the chirp rate–quadratic chirp rate distribution," *IEEE Trans. Geosci. Remote Sens.*, vol. 52, no. 11, pp. 7276–7289, Nov. 2014.
- [8] S. Shao, L. Zhang, and H. Liu, "An optimal imaging time interval selection technique for marine targets ISAR imaging based on sea dynamic prior information," *IEEE Sens. J.*, vol. 19, no. 13, pp. 4940–4953, Jul. 2019.
- [9] S. Shao, L. Zhang, J. Wei, and H. Liu, "Two-Dimension joint super-resolution ISAR imaging with joint motion compensation and azimuth scaling," *IEEE Geosci. Remote Sens. Lett.*, vol. 18, no. 8, pp. 1411–1415, Aug. 2021.
- [10] S. Shao, L. Zhang, H. Liu, P. Wang, and Q. Chen, "Images of 3-D maneuvering motion targets for interferometric ISAR with 2-D joint sparse reconstruction," *IEEE Trans. Geosci. Remote Sens.*, vol. 59, no. 11, pp. 9397–9423, Nov. 2021.
- [11] F. Pieralice, F. Santi, D. Pastina, M. Antoniou, and M. Cherniakov, "Ship targets feature extraction with GNSS-based passive radar via ISAR approaches: Preliminary experimental study," in *Proc. 12th Eur. Conf. Synthetic Aperture Radar*, 2018, pp. 1–5.
- [12] D. Pastina, C. Spina, and A. Aprile, "A slope-based technique for motion estimation and optimum time selection for ISAR imaging of ship targets," in *Proc. 14th Eur. Signal Process. Conf.*, 2006, pp. 1–5.
- [13] H. P. Sun, M. D. Xing, and L. J. Zhou, "Division of imaging intervals and selection of optimum imaging time for ship ISAR imaging based on measured data," in *Proc. CIE Int. Conf. Radar*, 2006, pp. 1–4.
- [14] J. D. Wang, L. Zhang, L. Du, B. Chen, and H. Liu, "Optimal coherent processing interval selection for aerial maneuvering target imaging using tracking information," *IEEE Sens. J.*, vol. 18, no. 10, pp. 4117–4128, May 2018.
- [15] T. S. Xiang, L. Wang, Z. X. Cao, and D. Y. Zhu, "Doppler-estimation based methods for airborne ISAR imaging of non-cooperative ship targets: Demonstration and analysis," in *Proc. 18th Int. Radar Symp.*, 2017, pp. 1–10.
- [16] G. Hajdúch, J. M. Le Caillec, and R. Garello, "Airborne high-resolution ISAR imaging of ship targets at sea," *IEEE Trans. Aerosp. Electron. Syst.*, vol. 40, no. 1, pp. 378–384, Jan. 2004.
- [17] D. Pastina, A. Montanari, and A. Aprile, "Motion estimation and optimum time selection for ship ISAR imaging," in *Proc. IEEE Radar Conf.*, 2003, pp. 7–14.
- [18] N. Li, L. Wang, and D. Zhu, "Optimal ISAR imaging time selection of ship targets using real data," in *Proc. IET Int. Radar Conf.*, 2013, pp. 1–4.
- [19] Y. Wang, X. Huang, and Q. Zhang, "Rotation parameters estimation and cross-range scaling research for range instantaneous doppler ISAR images," *IEEE Sens. J.*, vol. 20, no. 13, pp. 7010–7020, Jul. 2020.
- [20] Y. H. Du, Y. C. Jiang, Y. Wang, W. Zhou, and Z. Liu, "ISAR imaging for low-earth-orbit target based on coherent integrated smoothed generalized cubic phase function," *IEEE Trans. Geosci. Remote Sens.*, vol. 58, no. 2, pp. 1205–1220, Feb. 2020.
- [21] Y. Wang, R. Q. Xu, Q. X. Zhang, and B. Zhao, "ISAR imaging of maneuvering target based on the quadratic frequency modulated signal model with time-varying amplitude," *IEEE J. Sel. Topics Appl. Earth Observ. Remote Sens.*, vol. 10, no. 3, pp. 1012–1024, Mar. 2017.
- [22] M. Martorella and F. Berizzi, "Time windowing for highly focused ISAR image reconstruction," *IEEE Trans. Aerosp. Electron. Syst.*, vol. 41, no. 3, pp. 992–1007, Jul. 2005.
- [23] G. Li, T. Y. Zhang, Y. Li, Z. Ding, and M. Ke, "A modified imaging interval selection method based on joint time-frequency analysis for ship ISAR imaging," in *Proc. 12th Eur. Conf. Synthetic Aperture Radar*, 2018, pp. 1–6.
- [24] P. Zhou *et al.*, "Time-frequency analysis-based time-windowing algorithm for the inverse synthetic aperture radar imaging of ships," *J. Appl. Remote Sens.*, vol. 12, no. 1, pp. 1–20, Jan. 2018.
- [25] P. Zhou, X. Zhang, Y. S. Dai, W. Sun, and Y. Wan, "Time window selection algorithm for ISAR ship imaging based on instantaneous doppler frequency estimations of multiple scatterers," *IEEE J. Sel. Topics Appl. Earth Observ. Remote Sens.*, vol. 12, no. 10, pp. 3799–3812, Oct. 2019.
- [26] M. Y. Abdul Gaffar, W. A. J. Nel, and M. R. Inggs, "Selecting suitable coherent processing time window lengths for ground-based ISAR imaging of cooperative sea vessels," *IEEE Trans. Geosci. Remote Sens.*, vol. 47, no. 9, pp. 3231–3240, Sep. 2009.
- [27] Y. C. Jiang and S. Q. Yin, "Research on ISAR imaging method of parameter estimation based on optimal imaging period," in *Proc. 1st Int. Conf. Pervasive Comput. Signal Process. Appl.*, 2010, pp. 513–516.
- [28] Y. Hui, X. R. Bai, and F. Zhou, "JTF analysis of micromotion targets based on single-window variational inference," *IEEE Trans. Geosci. Remote Sens.*, vol. 59, no. 8, pp. 6600–6608, Aug. 2021.
- [29] R. Cao, Y. Wang, and Y. Zhang, "Analysis of the imaging projection plane for ship target with spaceborne radar," *IEEE Trans. Geosci. Remote Sens.*, pp. 1–21, Apr. 2021.
- [30] L. L. Du, Y. L. Xin, and Z. P. Chen, "A new algorithm for ship centerline extraction in ISAR image," in *Proc. 2nd Int. Conf. Adv. Comput. Control*, 2010, pp. 213–216.
- [31] X. Bai, R. Tao, Z. J. Wang, and Y. Wang, "ISAR imaging of a ship target based on parameter estimation of multicomponent quadratic frequency-modulated signals," *IEEE Trans. Geosci. Remote Sens.*, vol. 52, no. 2, pp. 1418–1429, Feb. 2014.
- [32] Q. Lv, T. Su, and K. Wu, "NUFFT-based parameter estimation algorithm for ISAR imaging of targets with complex motion," in *Proc. IET Int. Radar Conf.*, 2015, pp. 1–5.
- [33] N. Otsu, "A threshold selection method from gray-level histograms," *IEEE Trans. Syst., Man, Cybern.*, vol. 9, no. 1, pp. 62–66, Jan. 1979.
- [34] J. F. Wang and X. Z. Liu, "Measurement of sharpness and its application in ISAR imaging," *IEEE Trans. Geosci. Remote Sens.*, vol. 51, no. 9, pp. 4885–4892, Sep. 2013.



Rui Cao (Graduate Student Member, IEEE) was born in 1996. She received the B.S. degree in electronic information engineering from the Harbin Institute of Technology (HIT), Weihai, China, in 2018, and the M.S. degree in information and communication engineering in 2020 from HIT, Harbin, China, where she is currently working toward the Ph.D. degree in information and communication engineering.

Her current research interests include the field of ISAR imaging and radar signal processing.



Yong Wang (Senior Member, IEEE) was born in 1979. He received the B.S. and M.S. degrees in electronic engineering, and the Ph.D. degree in information and communication engineering from the Harbin Institute of Technology (HIT), Harbin, China, in 2002, 2004, and 2008, respectively.

He is currently a Professor with the Institute of Electronic Engineering Technology, HIT. His main research interests include the fields of time frequency analysis of nonstationary signal, radar signal processing, and their application in synthetic aperture radar

(SAR) imaging.

Dr. Wang was the recipient of the Program for New Century Excellent Talents in University of Ministry of Education of China in 2012, and the Excellent Doctor's Degree nomination Award in China in 2010. He has published more than 130 papers, most of them appeared in the journals of IEEE TRANSACTIONS ON GEOSCIENCE AND REMOTE SENSING, *IET Signal Processing*, *Signal Processing*, etc.



Chunmao Yeh received the M.S. degree in electronic engineering from the Harbin Institute of Technology, Harbin, China, in 2005, and the Ph.D. degree in electronic engineering from Tsinghua University, Beijing, China, in 2009.

In 2011, he joined Beijing Radio Measurement Institute, Beijing, where he is currently a Senior Engineer. His general research interests include radar system design, radar signal processing and imaging, radar anti-jamming, and automatic target recognition.



Xiaofei Lu was born in 1981. He received the B.S. and M.S. degrees from the Harbin Institute of Technology (HIT), Harbin, China, in 2002 and 2004, respectively, both in electronic engineering, and the Ph.D. degree in control theory and control engineering from Tsinghua University, Beijing, China, in 2012.

He is currently an Engineer with JiuQuan Satellite Launch Center, Jiuquan, China. His main research interests include the fields of target recognition, radar signal processing, and their practical application. He has published more than 20 papers.



Yun Zhang (Member, IEEE) was born in Heilongjiang, China, in November 1975. She received the B.S. and M.S. degrees in electronic engineering and the Ph.D. degree in information and communication engineering from the Harbin Institute of Technology (HIT), Harbin, China, in 2000, 2003, and 2009, respectively.

She is a Professor with the Research Institute of Electronic Engineering Technology, HIT. Her research interests include radar signal processing, synthetic aperture radar imaging, machine learning, and

pattern analysis in remote sensing.